Department of Physics
University College London

Preparatory work for C_3 line-list calculation

Author:
Santina La Delfa

Supervisor:
Prof. J. Tennyson

Thesis Submitted for M.Phil.

January 20, 2009

0.1 Abstract

The goal of this dissertation is to study the infrared absorption spectrum of the C_3 (carbon three) molecule. In particular, the aim is to investigate its ground electronic state up to 12.500 cm^{-1}, as this affects the atmospheres of cool C-rich stars.

The linear C_3 molecule shows very unusual properties for a linear molecule: a high degree of floppiness, no permanent dipole moment and a strong bent-stretch interaction. Consequently, the C_3 spectrum presents particular features such as overtones, hot bands, and, as has been recently detected in Carbon stars and molecular clouds, a quite low fundamental bending frequency (63 cm^{-1}) when in the ground electronic state. This dissertation aims to address each of these features.

The first section discusses the context for this work: the stars. It provides a brief introduction about the Astrophysics related to this research project. A review at the recent literature is provided and the experimental results which provide the goal for the results of the theoretical work in the rest of the dissertation are set out.

The second section introduces the C_3 molecule and outlines its properties. Previous C_3 studies are discussed and the theoretical approach used to study ro-vibrational spectra of triatomic molecules is set out. Preparatory tests and calculations are carried out to allow a theoretical reproduction of C_3 roto vibrational spectrum in the infrared region to be produced.

The third part of the thesis expands on the nuclear motion calculations of section 2 and presents the results of the large scale calculations performed using the DVR3D suit programs written by Tennyson *et al.* [1]. This program allows the calculation of energy levels, wave-functions, expectation values and Einstein Coefficients. It takes as input the Potential Energy Surface (PES) and a Dipole Moment Surface (DMS) constructed a priori (in section 2) by solving the electronic problem within the Born-Oppenheimer's approximation.

Because the quality of the PES sets the accuracy of the ro-vibrational calculations tests on different C_3 PESs and DMSs are performed. To reproduce accurate spectra of cool stars atmosphere in the temperature range of

$2000 - 4000$ K it was necessary perform calculations with high rotational quantum number. For this reason, tests with $J \gg 0$ were necessary to optimize the DVR3DRJZ parameters in order to guarantee a certain degree of accuracy and energy levels convergence.

The results of these calculations and associated C_3 line-lists should be very useful to support the observations and model atmospheric studies.

This work was generously supported by the QUASAAR Marie Curie Network.

Contents

Chapter 1

Modelling the Opacity of Cool Stars

The number of molecular species observed in space is about 140 and their formation is determined by the surrounding environment. Many of these species are found in the atmosphere of stars. Stars therefore, and in particular Carbon stars are the main target of this study.

In this section we discuss the properties of astrophysical environments. Our overall aim is to look at properties that will affect results from spectroscopy. Spectroscopy is the technique of analysing light coming from space to determine the properties of a remote object. Depending on the physical conditions of the particular environment under investigation, matter presents different structure, phase and composition.

We first introduce the method of spectroscopy before looking at the stellar parameters that affect it. The main ones will be brightness, radiation transfer and opacity effects. Finally we will give a brief explanation of stellar evolution and how the stellar parameters determine where in the evolutionary sequence a star is.

1.1 Molecular Spectroscopy

Molecular Spectroscopy is a technique for investigating the microscopic properties of molecules. Nowadays it is known to be the most powerful tool for finding detailed microscopic information about molecular systems. As such, many experiments and computational chemical investigations using this technique have been completed in the past few years.

A molecule is made up of a number of atoms and ions; these may be positive or negatively charged. The distribution of these charges create what is known as a dipole moment; a measure of the strength of charge and geometry of the molecule.

The basic principle behind Molecular Spectroscopy is that infra-red radiation (the electromagnetic spectrum with wavelength between 0.78 and 1000mm) is energetic enough to stimulate vibrations or rotations within a molecule. The alternating electrical field of the infra-red radiation interacts with fluctuations in the dipole moment of a given molecule. When the radiation matches the vibrational frequency of the molecule, radiation will be absorbed. This means that at this frequency there will be a reduced intensity of infra-red radiation. Each molecule therefore gives a characteristic "fingerprint"with varying intensities of radiation at different frequencies [2].

Every molecule possesses a unique spectrum or "fingerprint". This means that by looking at a series of "fingerprints "from a remote environment (a star for example) the molecular make-up of that environment can be determined. This means that qualitative and quantitative information about observed astrophysical objects such as planets, stars, interstellar medium, nebulae and so on can be determined.

In astrophysics, spectroscopy therefore sometimes represents a powerful tool for astrophysical investigation. For this reason it is really important know a-priori the features of a molecule to be able to identify it through spectra.

1.2 Stellar Parameters

1.2.1 Brightness

As you can see on a clear night – stars shine and some are brighter than others. In order to quantify this idea of brightness we consider the amount of energy emitted by a star that reaches us – the observer.

The amount of radiation at a given frequency ν coming from a star sited at distance d from the observer. The energy flux [3] is the rate of transfer of energy dE through a unit area S at a particular frequency ν *i.e.*

$$F_\nu = \frac{\mathrm{d}E}{\mathrm{d}\nu\,\mathrm{d}t\,\mathrm{d}S}. \tag{1.2.1}$$

The luminous power or intrinsic luminosity of a star of radius r at a given frequency ν is

$$L_\nu = 4\pi r^2 F_{\nu,S}, \tag{1.2.2}$$

where $F_{\nu,S}$ is the energy flux through the stellar surface S_1 see Figure 1.1.

If we imagine the star as a point and we consider the sphere centred on the star with radius d, the distance between the star and the observer, then all the energy emitted by the star that reaches the earth must pass through the surface of this sphere. The energy flux at the surface S_2 can be expressed by the equation:

$$F_{\nu,T} = \frac{L_\nu}{4\pi d^2}, \tag{1.2.3}$$

and from Equation 1.2.2 we can write it as:

$$\begin{aligned} F_{\nu,T} &= \frac{4\pi r^2 F_{\nu,S}}{4\pi d^2}, & (1.2.4)\\ &= \frac{r^2 F_{\nu,S}}{d^2}. & (1.2.5) \end{aligned}$$

Supposing that the radiation coming out from a stellar surface will travel through the empty space to reach the observer on earth, the observed brightness $F_{\nu,T}$ of a star will need to be adjusted for its size.

The solid angle under which a star is observed, $\Delta\Omega$, is a measure of how big that object appears to an observer looking from that point (see Figure 1.1) and can be expressed with the following equation:

$$\begin{aligned} \Delta\Omega &\approx \frac{S}{d^2}, & (1.2.6) \\ &\approx \frac{\pi r^2}{d^2}. & (1.2.7) \end{aligned}$$

We therefore define the intensity (or brilliance) of the radiation I_ν as the power radiated in a certain direction:

$$I_\nu = \frac{F_{\nu,T}}{\Delta\Omega}, \qquad (1.2.8)$$

Using Equations 1.2.5 and 1.2.7

$$I_\nu = \frac{F_{\nu,S}}{\pi}. \qquad (1.2.9)$$

As can be seen from equation (1.2.9), intensity is independent of the distance d between the star and earth.

The analytical description of radiation emitted from stars is based on comparative assumptions with "black body radiation". This is the radiation emitted by any object that has the property of absorbing any radiation that hits it at all λ and emitting the same amount of radiation it absorbs. As it neither gains nor loses energy a black body's radiation is therefore in thermodynamic equilibrium and it has a spectrum that depends only on its temperature T.

Experiments to reproduce and study black body radiation were performed in the 19^{th} century by Kirchoff. The radiation coming out from a small hole in the reflective walls of a hot cavity in thermodynamic equilibrium was used as an approximation of black body's radiation.

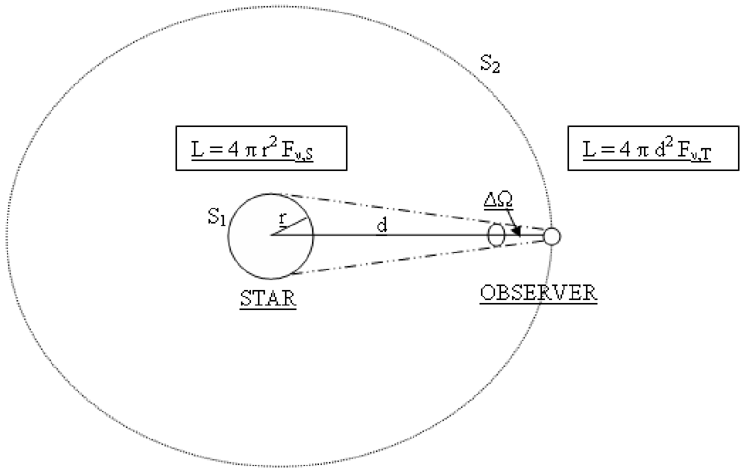

Figure 1.1: Schematic representation of the Star-Observer system.

Light in the cavity can be thought of as standing waves. The number of normal modes (resonant frequencies) of this oscillating system grows exponentially with the frequency. From a classical point of view, an oscillating system presents the same probability for all modes to be produced. However, it was observed in experiments that there were in fact less high frequency modes that the classical theory could explain. The only way to have a correct theorization of the experimental results was found by introducing quantum effects.

It was Planck who was the first to introduce quantum mechanics to explain the behaviour of light at high frequencies where the classical expression was not adequate. Using quantized modes, he showed that higher frequency modes are less probable than lower ones. Planck built an expression for the brilliance of a black body to explain correctly observations over the whole spectrum:

$$B_{\nu,T} = I_{\nu,BB} = \frac{2h\nu^5}{c^3} \frac{1}{e^{\frac{h\nu}{kT}} - 1}, \tag{1.2.10}$$

where ν is the frequency, h is Planck's constant ($6.626068 \times 10^{34}\mathrm{m}^2\mathrm{kg/s}$), k is Boltzmann constant ($1.3806503 \times 10^{23}\mathrm{m}^2\mathrm{kgs}^{-2}\mathrm{K}^{-1}$), c is speed of light ($3 \times 10^8\mathrm{ms}^{-1}$).

Integrating equation (1.2.10) over the whole range of frequencies, the Stefan law is obtained:

$$\int I_{\nu,BB} d\nu = \sigma T^4, \tag{1.2.11}$$

where $\sigma = 5,67051 \times 10^{-8}\mathrm{m}^{-2}W\mathrm{K}^{-4}$ is known as the Stefan-Boltzmann constant. Considering that $\nu = c \times \lambda^{-1}$ with c the speed of light and λ the wave length, it is possible to calculate the value of λ which corresponds to the maximum of radiance. This is obtained from equation (1.2.10):

$$\lambda_{max} = \frac{C}{T}, \tag{1.2.12}$$

where $C = 2.9 \times 10^{-3}\mathrm{m}K$ and T is the temperature expressed in Kelvin see Reference [4].

It is possible describe the brilliance of a star comparing it to the brilliance of an idealized black body.

$$I_{\lambda,STAR} = I_{\lambda,BB} \tag{1.2.13}$$

Therefore, from equation (1.2.9) the energy flux is given by

$$\begin{aligned} F_{\lambda,S} &= \frac{I_{\lambda,BB}}{\pi}, && (1.2.14) \\ &= C\left(e^{\frac{hc}{k\lambda T}} - 1\right)^{-1}, && (1.2.15) \end{aligned}$$

where $C = 2\pi hc^2/\lambda^5$.

From equation (1.2.15) we can calculate:

Temperature of Brilliance T_λ The temperature of a black body emitting, at wavelength λ, the same amount of radiation as detected from the star under investigation.

$$T_\lambda = \frac{\lambda^4}{2c}\frac{F_\lambda}{\pi}, \tag{1.2.16}$$

Surface Temperature T_{SURF} The temperature obtained using the equation (1.2.12) expressing the value of the wavelength corresponding to the maximum radiance:

$$T_{SURF} = \frac{C}{\lambda_{max}}, \tag{1.2.17}$$

with $C = 2.9 \times 10^{-3}\mathrm{m}K$.

Effective Temperature T_{Eff} The temperature obtained considering the radiance integrated over the whole range of wavelengths from equation (1.2.11):

$$T_{Eff} = \left(\frac{F}{\sigma}\right)^{\frac{1}{4}}, \tag{1.2.18}$$

where $\sigma = \dfrac{2\pi^5 k^4}{15c^2h^3}$ and h is Planck's constant, k is Stefan-Boltzmann constant, c is speed of light.

Results of Brightness Measurements

We have seen that from the measurement of brightness at different wavelengths that it is possible to discover various properties about remote bodies. In particular we have seen that the temperature and luminosity of a remote body can be inferred from these measurements. These two properties in turn can be used to determine which group a star belongs to.

Surface temperature and luminosity are the parameters used by Hertzsprung and Russell to classify stars into groups: main sequence; giant branch; white dwarf sequence; and very bright but rather cool stars known as supergiants (these groups will be discussed in greater detail in Section 1.3). This sequence is known as a H-R (Hertzsprung-Russell) diagram and is shown in Figure 1.2.

1.2.2 Transport Models

The radiation produced by nuclear reactions in a star's core passes through internal layers and emerges from the surface before travelling towards earth and the spectrometer we may use to look at the 'fingerprint' of the star.

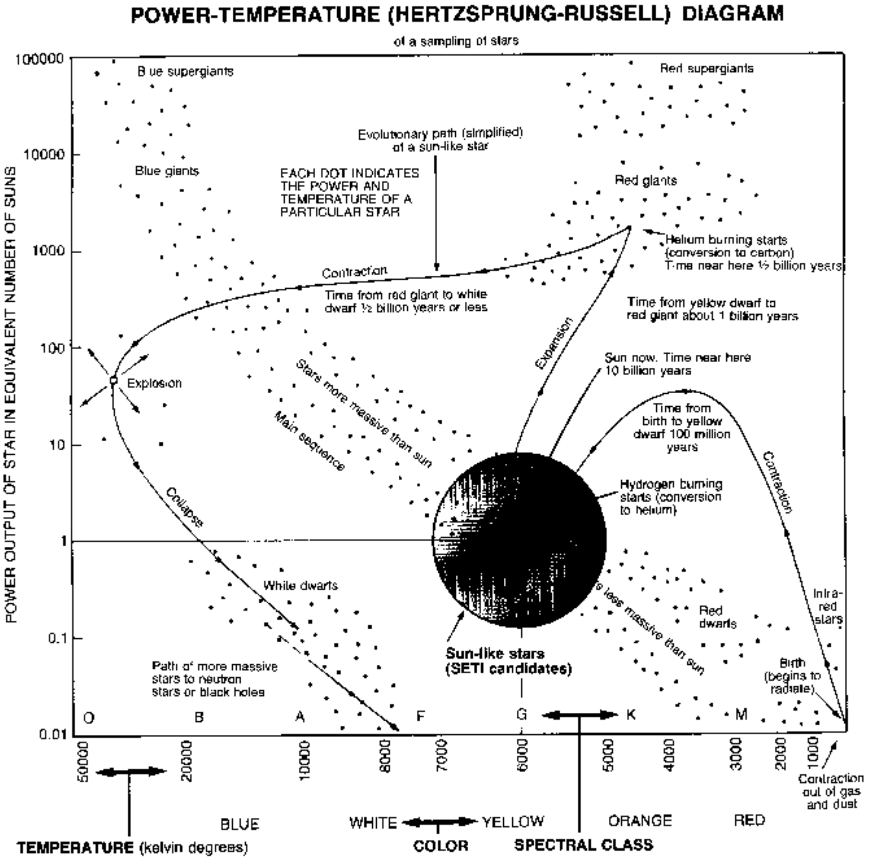

Figure 1.2: Hertzsprung-Russell Diagram from website www.bigear.org

The light, passing through internal layers experience several absorption and emission mechanisms [5]:

Electron Scattering happen when a photons' direction changes due to the interaction with electrons of the medium.

Free - Free (Bremsstrahlung) mechanism occurs when electrons interact with a positive electrical field and photons are emitted.

Bound - Free (photo-ionization) process is that mechanism happening when energetic photons are absorbed by atoms producing electron release.

Bound - Bound process is the absorption and successive reemission of photons by atoms or molecules.

Depending on the physical properties of the layers crossed, several energy transport processes may occur.

We discuss each of these processes in turn:

Radiative Transport High-energy photons are able to excite atoms which in turn generate lower energy photons. This process is called radiative transport and takes place on the surface layers of a star or near the core where high-energy photons are available.

Conductive Transport The heat of a star's core increases the kinetic energy of the material around it which will slowly diffuse towards the surface through particle collisions.

Convective Transport When the chaotic motion of heated material gains a preferential direction towards the surface, heat will be released to the cooler external layers and the cell will move back toward the centre, creating a circular motion known as convection.

Conduction is not an efficient transport mechanism in stars due to the much lower mean free path of particles respect to the photons and smaller speed of the particles [6].

Transport mechanisms are governed by a radial gradient depending on the temperature and pressure of the material defined by:

$$\begin{aligned}\nabla &= (\frac{\partial \ln P}{\partial \ln T}), && (1.2.19)\\ &= (1-\zeta)\nabla_R + \zeta\nabla_A, && (1.2.20)\end{aligned}$$

with P and T pressure and temperature; ∇_R and ∇_A the radiative and convective gradients respectively. ζ is a parameter measuring the convection energy transport efficiency and depends on the temperature, density, chemical composition and opacity of the material. It can take values: $0 < \zeta < 1$. Convection is a mechanism more efficient than radiative diffusion. The star needs to transfer the radiation produced in its nucleus to the external layers establishing the mechanism that is sufficient to maintain the mechanical stability (a balance between internal pressure and gravitational attraction). When the physical parameters of the stellar material such as temperature, density, chemical composition and opacity assume certain critical values, radiative diffusion is not anymore a mechanism sufficient to maintain stability; as consequence, convective transport is necessary. This competition between radiative and convective transport see equation (1.2.20) can be represented as follows:

$\zeta = 0$ $\nabla = \nabla_R$ Radiative diffusion is predominant.

$\zeta = 1$ $\nabla = \nabla_A$ Convection is predominant.

$\zeta \gg 1$ Radiative diffusion and convection are coexisting.

It is clear from above that when $\nabla \gg \nabla_R$ convection starts. This is known as the Schwarzschild criterion [5].

The energy transfer processes are very important in understanding the stars evolutionary process explained in Section 1.3.

The simplest model is to ignore the dynamic transportive effects (conduction and convection) and consider just the radiative transfer mechanism. As discussed at the beginning of this section, stellar spectra contain information about stellar atmospheric chemical abundances and physical conditions such as temperature and pressure. They are characterized by a continuum energy distribution with many absorption or emission lines (a drop or a spike in the continuum radiation at the associated wavelength).

However, we should be aware that spectra can show asymmetry in the line profiles. Time variability and doubling effects can occur as a result of is coupling effects between convective motion, radiation and instability. In this case the interpretation of the spectra becomes more complicated and the simple radiative transfer models excluding dynamical effects caused by convection are not reliable. In general however, models built just considering radiative transfer models are often used as approximation.

The Radiative Transport Model

The standard radiative transfer model is that based on the local thermodynamic equilibrium mentioned in the previous section where the radiation distribution curve of a star's atmosphere can be approximated by the Black Body (or Planck) curve.

When energy is transferred through radiative processes, photons diffuse random-walking through the atmospheric layers and experience scattering process (Compton scattering) due to the interaction of photons with electrons. This process is predominant when the interaction between radiation and matter is weaker. The direction of diffusion is towards lower temperature. This means that as the temperature decreases in the external layers, the density of the photons drops being proportional to T^3; This enhances the probability of process such as Bremsstrahlungh, photo-ionization, atomic and molecular absorption. The absorbed radiation is remitted and redistributing through scattering processes [7]. Scattered light disappears along the direction of observation and this corresponds to a drop of intensity in the spectrum. The interaction between radiation and matter can be described considering the drop in radiation intensity shown in Figure 1.3:

$$I_\lambda(h) = I_\lambda(h_0) + dI_\lambda(h_0). \tag{1.2.21}$$

The magnitude of the intensity variation depends on intrinsic properties of the material crossed and these are absorption and emission coefficients respectively κ_ν (in cm^{-1}) and ε_ν (in $erg\ cm^{-2}Hz^{-1}s^{-1}sterad^{-1}cm^{-1}$).

$$I_\nu(h) = I_\nu(h_0) - \kappa_\nu I_\nu(h_0)dh + \varepsilon_\nu dh, \tag{1.2.22}$$

$$dI_\nu(h) = -\kappa_\nu I_\nu(h_0)dh + \varepsilon_\nu dh. \tag{1.2.23}$$

Integrating from h_0 to h:

$$\int dI_\nu(h) = \int -\kappa_\nu I_\nu(h_0)dh + \int \varepsilon_\nu dh, \tag{1.2.24}$$

and considering that under the black body approximation the relation between absorption and emission coefficient is given by:

$$\frac{\varepsilon_\nu}{\kappa_\nu} = B_{\nu,T}. \tag{1.2.25}$$

Equation (1.2.23) becomes:

$$I_\nu(h) = I_\nu(h_0)e^{-\kappa_\nu \Delta h} + B_{\nu,T}\kappa_{\nu,T}\Delta h, \tag{1.2.26}$$

where the first term is the Lambert-Beers' expression that describes how intensity decreases when radiation crosses a layer of thickness Δh with absorption coefficient κ_ν (cross section times the number of absorbers) at temperature T (see Figure 1.3). It represents the absorption due to the intrinsic properties of the material crossed. The second term takes into consideration also the thermal properties of the layer crossed.

Opacity

Opacity is the resistance that atmospheric layers make to the passage of electromagnetic radiation coming from the stellar interior. This property strictly depends on the physical conditions and chemical abundances. For example, the temperature is lower in outer stellar layers, this increases the abundances of atomic and molecular species and as a result the opacity is greater.

It is important to introduce the “opacity parameter for a better description of the atmospheric absorption in stars keeping into account all the physical processes that can happen at a particular height characterized by certain physical parameters. It is expressed by the following equation:

$$K_\nu = \frac{\kappa_\nu}{\rho}, \tag{1.2.27}$$

with κ_ν the absorption coefficient and ρ the material density. Opacity represents the cross section of all the physical processes that might occur and can depend on the temperature, density and chemical composition of the layer.

The total opacity is the sum of terms describing the single opacities coming from each of the physical process occurring and already described in Section 1.2.2. Introducing a parameter called "Resistivity "(χ) we can write:

$$\chi = \frac{1}{K_{\nu,TOT}} = \frac{1}{\kappa_{\nu,Scatteringe-}} + \frac{1}{\kappa_{\nu,free-free}} + \frac{1}{\kappa_{\nu,bound-free}} + \frac{1}{\kappa_{\nu,bound-bound}} \tag{1.2.28}$$

This expresses the resistance of the material to the passage of the radiation in analogy with electrical resistances put in parallel and opposing to the passage of electricity.

$\kappa_{\nu,Scattering}$ is the opacity due to the electron scattering processes (or the Compton Effect). It depends on the concentration of Hydrogen atoms that give us a measure of the availability of free electrons and it is predominant in internal stellar layers where there are high values for the temperature and low density conditions.

At higher densities the major contributors to the total opacity are free-free (Bremsstrahlung) and the photo-ionization processes expressed by

$\kappa_{\nu,free-free}$ and $\kappa_{\nu,boun-free}$ both depending on the temperature $T^{-3.5}$ and density ρ. The temperature decreases going towards outer star layers *i.e.* $\mathrm{d}T/\,\mathrm{d}h$ and Bound-Bound processes become an important opacity source:

$\kappa_{\nu,bound-free}$ depending on $T^{-2.5}$ and density $\rho^{0.5}$.

Analysing the intensity profile of the radiation at a certain wavelength, it is possible to calculate from which depth the radiation is coming from (see Figure 1.4).

Atmospheric models can therefore be constructed using the temperature T and density ρ at different heights h as input and the abundances varied until computed and observed spectra coincide.

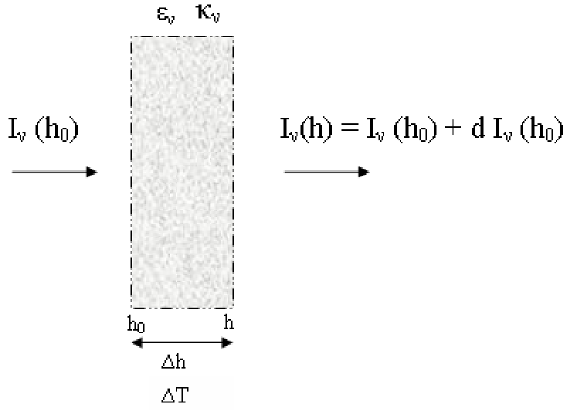

Figure 1.3: Schematic representation for two adjacent atmospheric layers at distance Δh apart with temperature difference ΔT.

Line-opacity

We have described the radiation intensity parameterized in terms of the opacity of the material κ_ν. The absorption and emission of light by the material is determined by the quantum mechanics of the constituents. A material system subjected to irradiation will absorb photons changing its energy status.

An atom in the outer layers of a star when hit by a photon of a specific frequency will change its energy status by a specific amount. This absorption is known as line-opacity. The relation between energy level populations

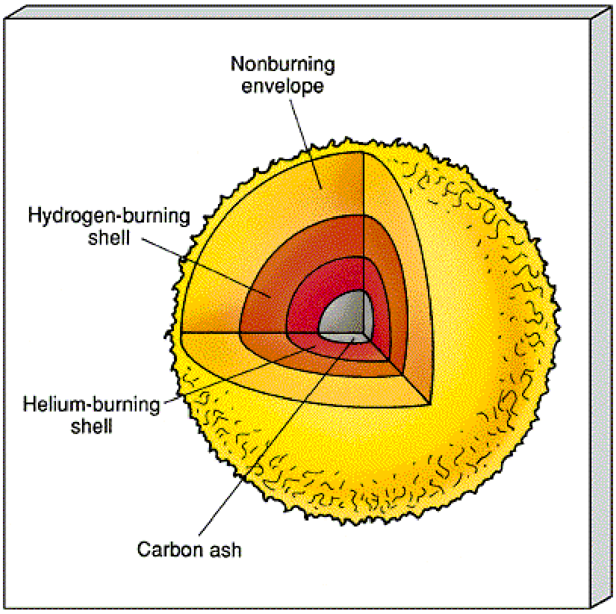

Figure 1.4: Layers of an Asymptotic Giant Branch (AGB) star (taken from *www.shef.ac.uk*)

corresponding to the number of molecules that in that instant occupy that particular energy state, assuming a local thermodynamic equilibrium can be described by the Maxwell−Boltzmann distribution:

$$\frac{N_m}{N_n} = \frac{g_m}{g_n} \exp\left(-\frac{\chi_{m,n}}{kT}\right), \tag{1.2.29}$$

where g_i is the statistical weight of the $i = n$ and m levels, $\chi_{m,n}$ is the difference in energy levels, T is the temperature, k the Boltzmann constant and N_i is the occupation number of the energy level $i = n$ or m. If a volume V containing molecules is immersed in an electromagnetic field, the number of energy levels for unity of volume is:

$$s = \frac{8\pi\nu^2 d\nu}{c^3}, \tag{1.2.30}$$

and the occupation number w is [4]:

$$w = \frac{s}{\exp^{\frac{-h\nu}{kT}} - 1}, \tag{1.2.31}$$

The density energy is:

$$\begin{aligned} U_\nu d\nu &= \nu w & (1.2.32) \\ &= \frac{8\pi hc\nu^3 d\nu}{\exp\left(-\frac{h\nu}{kT}\right) - 1}. & (1.2.33) \end{aligned}$$

Absorption and emission processes between two generic energy levels E_n and E_m can be explained using the Einstein coefficients. Einstein introduced some parameters known as A_{mn}, B_{mn} and B_{nm} expressing respectively the probabilities for spontaneous emissions, induced emission and absorption between energy levels. The relation between these processes is:

$$N_n B_{nm} U_\nu = A_{mn} N_m + U_\nu B_{mn} N_m, \tag{1.2.34}$$

Extracting the density of energy U_ν from the above equation, using equation (**??**) and comparing it with the density energy expressed by (**??**), we obtain the relation between Einstein parameters:

$$A_{nm} = 8\pi hc\nu^3 B_{nm}, \tag{1.2.35}$$

Opacity is not a directly observable quantity but is instead determined by the energy levels and occupation numbers (or Einstein coefficients) of the constituent parts of an atmospheric layer.

Line strength

When the radiation electro-magnetic field interacts with the dipole moment of a molecule it produces a transition. The line strength associated with this transition is

$$S(m \leftarrow n) = \sum_{\phi_m,\phi_n} \sum_{A=X,Y,Z} |< \phi_m \mid \widehat{\mu_A} \mid \phi_n >|^2, \tag{1.2.36}$$

where ϕ_m and ϕ_n are eigenfunctions corresponding to energy levels E_m and E_n. μ_A is the dipole moment operator with respect to the $A = X, Y, Z$ molecular coordinate system.

The notation

$$\int \phi_m^* O_p \phi_n \, \mathrm{d}^3 r = |< \phi_m \mid \widehat{O_p} \mid \phi_n >| \tag{1.2.37}$$

denotes the transition moment integral where O_p is the transition moment operator. The transition moment operator represents a function that operates on a quantum state represented by wave function ϕ_n to reproduce another state ϕ_m. Note that the squares of the absolute values $\mid \phi \mid^2$ give the probability distribution that the system will be in any of the possible states. In this case the operator is the molecular dipole moment and performs the transition between two vibro-rotational states of a molecule.

Note also that

$$\sigma \propto |< \Psi_m \mid \widehat{O_p} \mid \Psi_n >|^2 \propto A_{mn}, \tag{1.2.38}$$

where σ is the cross section (in this case it represents absorption probability of photons by molecules) and A is the Einstein coefficient for spontaneous decay. So the intrinsic line strength will be proportional to both σ and A.

The absorption coefficient is calculated under the thermal equilibrium approximation using the equation

$$I(m \leftarrow n) = \frac{8\pi^3 N_A \nu_{nm} exp(-\dfrac{E_m}{kT})[1 - exp(-\dfrac{h\nu_{nm}}{kT})]}{(4\pi\varepsilon_0)3hcQ} S(m \leftarrow n), \tag{1.2.39}$$

where $h, c, k, N_A, \varepsilon_0$ are respectively Planck's constant, the speed of light, Boltzmann's constant, Avogadro's number and magnetic permeability in vacuum. ν_{nm} is the transition wave number (cm^{-1}) corresponding to the energy levels E_m and E_n and Q the partition function describing the statistical properties of a system of particles in thermodynamic equilibrium at temperature

T distributed over w energy levels E_w with degeneracy factor g_w. It is given by

$$Q = \sum_w g_w exp(-\frac{E_w}{kT}). \tag{1.2.40}$$

Line Lists

A line list is a measure of opacity at a given wavelength and gives a molecule's "fingerprint". When no line list is available for a specific molecule then we can build one considering the quantum properties of the molecule.

A spectral line originates in the photosphere of a star and its absorption is usually measured relative to the flux mean opacity over the continuum.

Using a line list it is therefore possible to calculate molecular abundances in a star. However, in order to interpret a star's line list an accurate representation of a line list for each molecule must be available. As we shall see, in the case of C_3 (which is not abundant on earth) such a line list must be calculated theoretically.

Weak Lines

For higher energies where the number of absorption systems in a particular spectral range is fewer, the line absorption coefficient will be relatively small and it will result in a ‶weak line ″.

It turns out that even though they are weak, these lines play an important role and must be included in any reliable atmospheric model. Even though weak lines do not significantly contribute to the absorption coefficient integrated over the whole spectrum, they can change the stellar model atmosphere structure by several orders of magnitude due to the relatively big change of the (still weak) absorption in selected intervals of the spectrum (see Jorgensen *et al.* [8]).

1.3 Stellar Evolution

This section describes evolutionary processes in stars. It is necessary to understand these processes in order to better describe stellar spectra features [5].

1.3.1 The Beginning – A Dust Cloud

Material in the universe such as simple molecules and grains are constantly subject to random fluctuations in pressure, temperature and density due to evolutionary events happening across the whole universe. This continuous compression and rarefaction motion can sometimes develop into a growing instability where the increase of density is maintained and enlarged. In fact, attraction between molecules or grains is governed by two fundamental forces

- **Gravitational law** The force between two bodies F_{GRAV} is given by

  $$F_{GRAV} = G\frac{mM}{r^2}, \tag{1.3.1}$$

  where m and M are the masses of the two bodies respectively, r is the distance between them and G is the gravitational constant.

- **Pressure** The force due to the change in pressure p with radius is given by

  $$F_{PRESS} = -\frac{m}{\rho}\frac{\mathrm{d}p}{\mathrm{d}r}, \tag{1.3.2}$$

  where ρ is the density of the material.

In hydrostatic equilibrium these forces balance so that:

$$\frac{dp}{dr} = -G\frac{\rho M}{r^2}. \tag{1.3.3}$$

The high density values leads to a local gravitational collapse of the surrounding material. In fact, when the mass of the material reaches a critical value known as Jean mass, the kinetic energy of the material is not able to resist the gravitational collapse, leading to the stellar formation begins.

The Jeans mass depends on the temperature and density of the material as shown below [5]:

$$M_J = (\frac{5k}{G\mu m_u})^{\frac{3}{2}}(\frac{3}{4\pi})^{\frac{1}{2}}T^{\frac{3}{2}}\rho^{-\frac{1}{2}}. \tag{1.3.4}$$

It describes how a decrease in temperature reduces the critical value for the Jean mass and the probability for the cloud collapse enhances.

1.3.2 From Protostars to the Main Sequence

During the emission processes (as energy is being radiated away) temperature, internal energy and therefore pressure decrease. Equation (1.3.3) says that the gravitational force must increase to try to balance this reduction in pressure. This means that more material from the surroundings fall to the centre of this newly formed spherical gas cloud which is called a protostar. During this stage, called pre-main sequence, a star's luminosity is high enough to allow it to be detected. In this stage pulsating motions are observed due to a structural stabilization process still ongoing. Stars in this stage have some peculiarities that allow them to be recognized and classified as T Tauri stars.

The opacity of the material starts to increase, until emission of radiation in the VIS (visible region) is totally prevented; The cloud follows its collapse and the gravitational energy becomes more negative as a consequence of material contraction. When the rise in opacity prevents emission in the IR (Infrared region) the contraction ends (the stellar radius becomes constant) and the kinetic energy of free fall is converted into internal heat. A shock wave spreads across the external layers raising the temperature and the stellar luminosity. The ionization process starts and the star evolves on the Hayashi track in the H-R Diagram. During this stage the convective mechanism ($\nabla > \nabla_A$ see Section 1.2.2) to transport energy from the centre to the surface is necessary in order to re-establish "Virial equilibrium "that occurs when the energy released from the gravitational contraction is half of the energy required for the ionization processes. As result, the superface temperature and radius of the star are almost constant. Convective contraction follows through equilibrium stages. The stellar radius decreases and the temperature starts to rise until the radiative transport mechanism becomes predominant. The star is now in the stage denoted as Henyey track in which the luminosity is approximately constant and the core temperature of the star keeps on growing. The star is now approaching the Main-Sequence stage.

Jumping the Main Sequence!

- For stars with masses less than 0.05 $M_\odot$ (where $M_\odot$= solar mass = $1.98892 10^{30}$ kg), core temperatures will never be high enough to activate nuclear reactions and gravitational contraction will result in a drastical increase in density towards the centre. Electrons in the core will occupy, in pairs, the lowest energy state available and they will be frozen into a kind of crystalline pattern. When a total degenerate state is reached, no internal heat is produced; contraction stops and protostars go directly into the white dwarf stage without passing through the main sequence.
- Rare stars with masses greater then 50 $M_\odot$ will not go through the main sequence stage. They are identified as super massive objects with evolutionary tracks that are still not clear.

1.3.3 Main Sequence

During the Pre-Main sequence stages the main source of energy in a star is the gravitational contraction. This raises the core density and temperature up to critical values where nuclear reactions occur.

When nuclear reactions are steadily active in the core the star is officially on the track denoted as the Main-Sequence. Those points in the evolutionary curve at which the star contraction ends and hydrogen burning starts, define the zero−age main sequence (ZAMS). A star's evolutionary curve maps how surface temperature and luminosity vary with time (H-R diagram). This curve will cross the H-R diagram (discussed in Section 1.2.1) at a certain position depending on the initial mass and chemical composition of the initial gas cloud.

Stars with higher mass and lower values of metallicity cross the ZAMS at higher values of luminosity and temperature (the left high-side of the H-R diagram). This is because when the metallicity of stars is lower, the opacity and UV absorption decrease and the values for the temperature and the luminosity increase.

Nuclear Fusion

Two different processes can occur in the core of stars to transform Hydrogen (H) into helium (He):

- **PP process** Conversion of hydrogen into helium through three different branches where the last two produce beryllium (Be).
- **CNO process** Conversion of hydrogen into helium through a combination of carbon (C), nitrogen (N) and oxygen (O).

Unlike the CNO mechanism, the PP (proton-proton) process does not have a strong dependence on temperature and as a result the H-burning region is much more extended around the core; Nuclear reactions release an amount of energy that needs to be transported efficiently through radiative or convective transport to the external layers in order to assure the thermo-mechanical stability of the star: a balance between the amount of energy produced in the core, the amount dispersed in the interstellar medium through the surface and the gravitational energy.

Mass is also the decisive parameter in determining the heat transport behaviour (see Section 1.2.2) during a star's time on the main sequence. In stars with a mass:

- $M < 1.1\mathrm{M}_{\odot}$ **with a Radiative core**(in which the PP process is predominant) an extensive area around the nucleus is permeated by radiative transport mechanisms and just a thin surface layer shows a predominance of the convective transport mechanism.

- $M > 1.1\mathrm{M}_{\odot}$ **with a Convective core**(in which the CNO process is predominant) a small area of convection around the nucleus is present and an extended layer where the radiative transport mechanism is predominant.

Stars are formed by concentric layers over the core. These are:

- The Photosphere
- The Chromosphere
- The Corona

Solar-type stars (see Figure 1.4) have convective envelopes and a lower surface temperature than those stars with a convective core; they can possess chromospheres and coronas accompanied by a stellar wind.

The star then reaches a stable phase where there is a balance between internal pressure (gas and radiation pressure) and gravitational attraction. For each value of the mass of a star it is possible calculate the "Eddington limit"; this is the value of the luminosity for which gravitational pressure equals the radiation pressure.

During H-burning the core radius decreases leading to increase in stellar luminosity and radius.

1.3.4 The End

After billions of years the hydrogen in the core of a star is exhausted and it no longer has a source of nuclear energy to balance gravitational contraction. After the main sequence stage stars will follow a different evolutionary path depending on their masses. If the mass of the star is:

1. $\mathbf{M} < \mathbf{2.5}\ \mathrm{M}_{\odot}$ after Hydrogen exhaustion in the core, the star goes through several stages and processes such as the red giant branch stage; helium-burning; asymptotic giant branch stage; and it will end up as a

planetary nebulae and white dwarf. This evolutionary curve is shown in Figure 1.5.To describe more in detail the evolutionary stages for this group of stars: depending on the mass the star will have two different structures (respectively with a radiative or a convective core) during the H-burning stage.

- **M $<$ 1.4 $M_\odot$ with a Radiative core,** H-burning processes are faster in the centre of the star and the energy released is transported through radiative mechanisms. The absence of convective motions and mixing of the material lead to a continuous decrease of the quantity of hydrogen in the nucleus up to hydrogen exhaustion and the subsequent formation of an inert helium core. An isothermal status is established and the central density rises to balance external pressure. The density growth is opposed by a partial core degenerate condition. A thin shell around the inert helium-nucleus warms up and H-burning reactions are activated. This shell is the source of energy for promoting the expansion of external layers; this results in a to the stellar radius increase, density and superficial temperature decrease, superficial opacity growth and convection activation. Convective motions are responsible for the process called dredge-up where material is stirred and reaction products are transported to the outer layers. Luminosity will increase and the star reaches the red giants branch (RGB).
- $1.4M_\odot < M < 2.5M_\odot$ **with a Convective core,** differences to the low mass case exist; the hydrogen burning rate is constant in all parts of the core thanks to convective stirring. This leads to the formation of an isothermal and inert helium core; this contracts so that the central temperature rises the central temperature and H-burning is activated in a shell surrounding the core. The star envelope expands and the star will evolve towards the red-giant branch (RGB).

During the RGB stage, the convective motion provides hydrogen to the internal layers of the star where H-burning is still active. As a consequence the temperature increases, the mass of the helium nucleus is enhanced and it starts to contract. The core temperature rises and helium starts to burn fast in the core under degenerate conditions (He flash). This stage is indicated as Zero Age Horizontal Branch or ZAHB.

When helium is exhausted, the Carbon-Oxygen nucleus contracts and the stellar envelope expands leading to an increase in luminosity. The star moves onto the Asymptotic Giant Branch (AGB) track where thermonuclear runaway processes will be responsible for what is called a 'Thermal Pulse'. The luminosity and radius will increase and the temperature decreases below the value necessary for hydrogen burning. Convective motions will extends to the inner regions causing dredging up of carbon atoms towards the outer atmospheric layers where carbon will then become more aboundant than oxygen and the H-shell will continually supply the necessary quantity of helium for the next thermal pulse.

This process causes mass loss from the surface and the H-shell becomes unstable as the star starts to pulsate. When the envelope mass decreases to under 0.001 $\mathrm{M}_\odot$ the mass loss ends and super winds obscure totally the star. In the H-R diagram the star moves towards the Post-AGB phase where the AGB outflow will form a planetary nebula. Finally the star's core cools down atconstant radius. This is known as the white dwarf stage.

The second group of stars are those with masses between:

2. **$\mathbf{2.5}\mathrm{M}_\odot < \mathbf{M} < \mathbf{8}\mathrm{M}_\odot$ with Convective cores.** The evolutionary path up to the red giant branch stage is the same as the ones described for stars with masses $M < 2.5\mathrm{M}_\odot$ and with a convective core. After the RGB phase the star shows: helium-burning,the blue loop, dredge up, asymptotic giant branch stage, thermal pulsing.Until the conditions allow explosive phenomena well known as Supernovae (see Figure 1.6).

   Let us describe in more details the processes after the RGB stage. When the inert helium core reaches the Schoenberg-Chandrasekhar limit ($M_{He} > M_{CH} = 1.4\mathrm{M}_\odot$) , the core will contract rapidly and the temperature will increases to activate (ignite) helium burning (10^8K) in the core and hydrogen burning in shells around it. The radius of the star's envelope increases drastically and the surface temperature decreases. The hydrogen burning processes in the shells around the core result in an increase of the superfice temperature whilst the luminosity remains constant. The star is tracking the stage known as the Blue Loop. When the helium-burning process ends, the star has a inert Carbon-Oxygen nucleus and shells burning hydrogen and helium

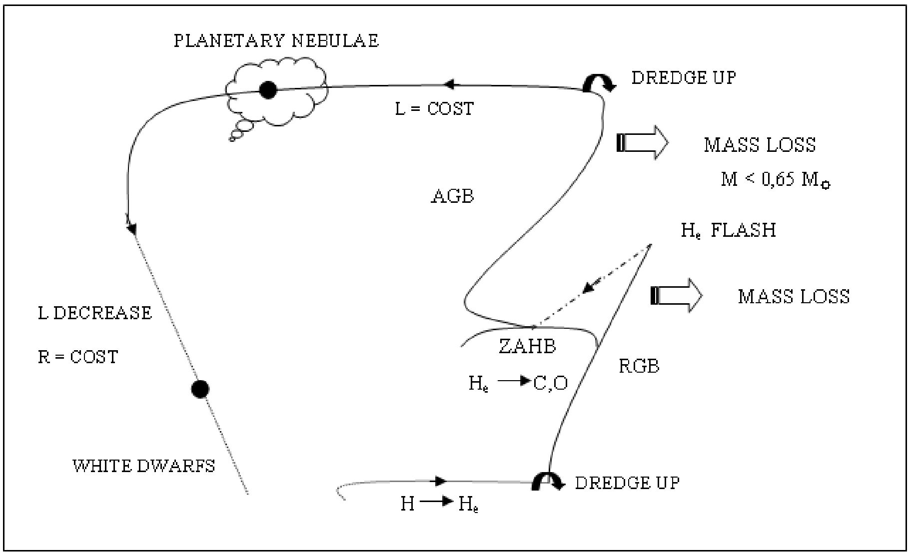

Figure 1.5: Schematic representation of the evolutionary track for stars with $M < 2.5$ $\mathrm{M}_{\odot}$

around it. The core starts to contract again, the radius increases and the surface temperature decreases. This leads to an increase in opacity and to the activated of convection motions. Another dredge up process is activated at the end of the blue loop. This mixing provides the core with new helium atoms to burn and nuclear reactions again start in the core. The luminosity increases and the star moves towards the AGB stage where the star exhibits thermal pulsing processes and mass loss. At this point the final destiny of the star is different and depends on the remaining mass of the core after the thermal pulsing. In fact if:

- $M > M_{CH} = 1.4\mathrm{M}_\odot$

  The mass reaches the Schoemberg-Chandrasekhar limit

  The C-O nucleus collapses and an explosive C-burning process starts up to expel all the outer envelope of the star. This is a supernova.

- $M < M_{CH} = 1.4\mathrm{M}_\odot$

  The mass is below the Schoemberg-Chandrasekhar limit

  The star evolves as a planetary nebula and becomes white dwarf. If the star is not in a binary system the cooling-off could lead to a supernovae explosion. If the star is part of a binary system, mass can be transferred between the two stars. This mass transfer allows the core to reach the Schomberg-Chandrasekhar limit; carbon deflagration occurs and the star will end up as a supernova.

3. **M** $>$ **8**$\mathrm{M}_\odot$ H-burning carries on with carbon-burning up to silicon and beyond to iron. When the iron core mass has exceeded the Chandrasekhar limit, it will collapse forming a neutron star or a black hole.

1.4 Cool Carbon Rich Stars and Stellar Opacity

Stars which are rich in carbon ($C : O \gg 1$) and have an extended atmosphere (those in the Asymptotic Giant Branch (AGB) stage) have very low densities and their photospheres are cool enough (less then about 4500 K) to allow molecules to form.

An example of these characteristics can be found in those stars classified as the Mira variable type. This type of stars presents other peculiarities such as: excess brightness in the infra-red spectrum; pulsations; mass loss; emission lines (hydrogen, silicon and iron); absorption lines (metals) and molecular absorption bands.

A very peculiar and interesting dynamics exists in the atmospheres of stars during the AGB evolution phase. Energy from the inner layers is transferred to the surface by the convection mechanism (as discussed in Section 1.2.2).

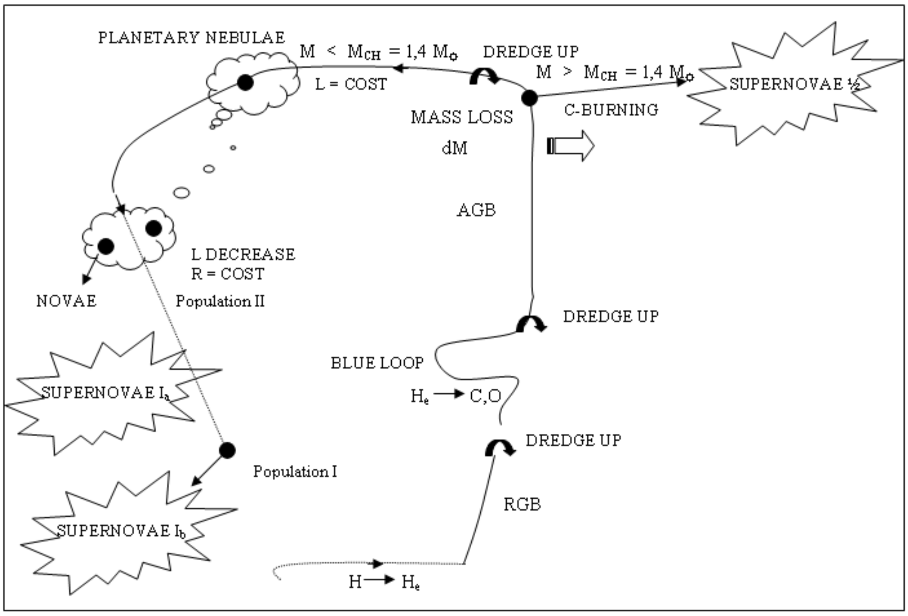

Figure 1.6: Schematic representation of the evolutionary track for stars with $2.5\mathrm{M}_{\odot} < M < 8\ \mathrm{M}_{\odot}$

This creates irregular pulsations with shock waves propagating towards the surface where matter is expelled as wind.

As a consequence spectra of AGB star atmospheres are very complex showing an enormous number of atomic and molecular lines. A radiative-hydrodynamic model inclusive of coupling effects between convective motion, radiation and instability effects is necessary to explain the asymmetries in the line profiles, time variability (due to the Doppler effect) and doubling effects. Theoretical calculations can help in the analysis of the observations, not just predicting the line positions but also giving fundamental coefficients (such as intensities)

[9].

This report presents the preliminary work carried out to perform a computational study of the C_3 system in order to obtain an accurate and complete line list to test against experimental results and astronomical observations of AGB stars.

Chapter 2

Molecular Properties of the C_3 Molecule

In recent years, there has been increasing interest in pure carbon molecules, sometimes referred to as polycarbons or C_n (see for example Weltner and Van Zee [10]). New experimental methods have been developed to study the quite peculiar and complex spectroscopic properties of these C_n species up to $n = 200$.

At the moment, there are just few observations of C_n species in space. C_3 and C_5 have been detected in comets, the diffuse interstellar medium and in the circumstellar shells, of some late type giant carbon stars (see Section 1.3) [11].

The C_3 molecule plays an important role in the growth of carbon chains and the determination of its abundance in the interstellar and circumstellar media could improve our understanding of the chemistry prevailing in these objects [12].

The $^{12}C_3$ molecule is formed of three symmetrically equivalent boson nuclei. This means that the total spin of the particles forming nuclei of carbon is an integer.

2.1 Coordinate Systems and Notation

Before looking at the properties of the molecule it is important to establish the various notations and coordinate systems used:

Notation

Coordinate Systems

It is convenient to describe the molecule using a Cartesian coordinates reference system (x, y, z) centred on the centre of mass of the molecular system as shown on the Figure 2.1.

The symmetric and antisymmetric stretch coordinates coordinate system is (X_1, X_2, θ) with $X_1 = q_1 + q_2 - 2r_e$ as the symmetric stretch coordinate, $X_2 = q_1 - q_2$ is the antisymmetric stretch coordinate where q_1, q_2 are the two bond-lengths, θ the angle between bonds and r_e is the bond-length at equilibrium configuration.

Jacobi or scattering coordinates r, R and α are $r = q_2$, R is the distance between q_2 centre of mass and the other carbon atom - see Figure 2.1.

2.2 Rotation-Vibration Spectra

Using Infrared Spectroscopy (IR) (see Section 1.1) it is possible to study the vibrational and rotational frequencies of triatomic molecules which correspond to discrete energy levels. We discuss each of these in turn.

2.2.1 Vibrational Frequencies

A molecule with n atoms can vibrate in $3n - 6$ normal modes. Linear triatomic molecules have $3n - 5$ modes (if $n = 3$ it has 4 vibrational modes) Figure 2.2 . We label these:

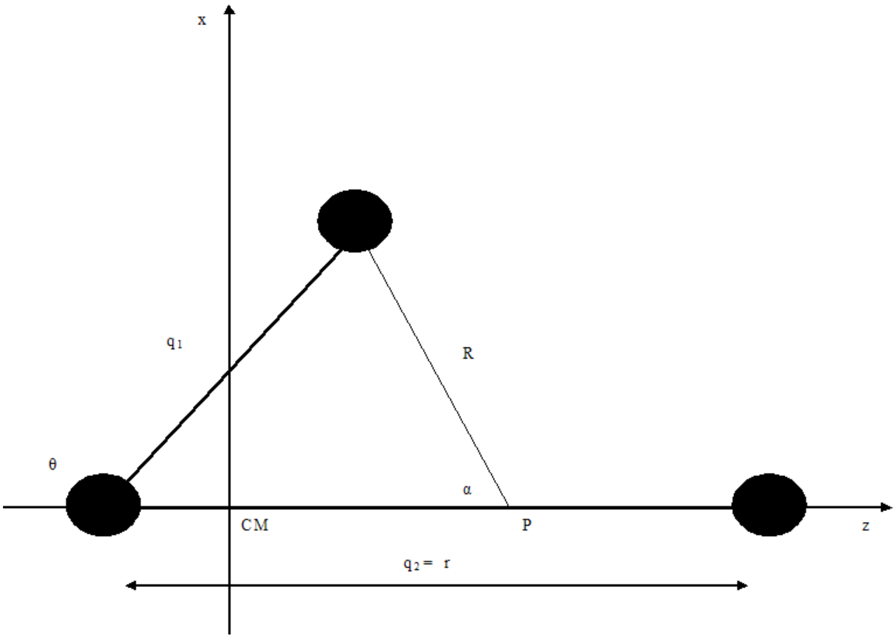

Figure 2.1: The bond-length coordinate system (q_1, q_2, θ) and Jacobi coordinates (r, R, α) chosen to study C_3. The z axes of the Cartesian system (x,y,z) is embedded along the q_2 bond-length.

- Symmetric-stretching (parallel to the linear axis)
- Anti-symmetric stretching (parallel to the linear axis)
- Bending (perpendicular to the linear axis and double degenerate indicating the two directions in which the molecular system bends).

In terms of spectra (working in a Cartesian coordinate system (x, y, z)) these vibrational modes are called:

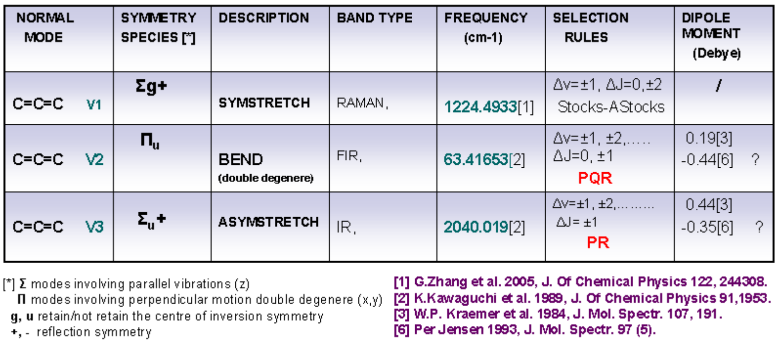

NORMAL MODE	SYMMETRY SPECIES [*]	DESCRIPTION	BAND TYPE	FREQUENCY (cm-1)	SELECTION RULES	DIPOLE MOMENT (Debye)
C=C=C V1	$\Sigma g+$	SYMSTRETCH	RAMAN,	1224.4933[1]	$\Delta v=\pm1$, $\Delta J=0,\pm2$ Stocks-AStocks	/
C=C=C V2	Π_u	BEND (double degenere)	FIR,	63.41653[2]	$\Delta v=\pm1, \pm2, \ldots$ $\Delta J=0, \pm1$ PQR	0.19[3] -0.44[6] ?
C=C=C V3	Σ_u+	ASYMSTRETCH	IR,	2040.019[2]	$\Delta v=\pm1, \pm2, \ldots$ $\Delta J=\pm1$ PR	0.44[3] -0.35[6] ?

[*] Σ modes involving parallel vibrations (z)
Π modes involving perpendicular motion double degenere (x,y)
g, u retain/not retain the centre of inversion symmetry
+, - reflection symmetry

[1] G.Zhang et al. 2005, J. Of Chemical Physics 122, 244308.
[2] K.Kawaguchi et al. 1989, J. Of Chemical Physics 91,1953.
[3] W.P. Kraemer et al. 1984, J. Mol. Spectr. 107, 191.
[6] Per Jensen 1993, J. Mol. Spectr. 97 (5).

Figure 2.2: C3 Table showing C_3 fundamental modes' properties.

- Parallel bands: The anti-symmetric and symmetric stretching motion parallel to the z molecular axis.
- Perpendicular bands: The perpendicular bending motion along x, y axes.

Within the harmonic oscillator approximation, the vibrational energy levels of a molecule are given by:

$$E\left(\nu_i\right)=\sum_i h\nu_i\left(\nu_i+\frac{d_i}{2}\right), \tag{2.2.1}$$

where d_i is the degeneracy of the i^{th} mode with frequency ν_i and h is Planck's constant.

A simple way of describing vibrational motions is to treat them as harmonic oscillator systems with actual potential energy and dipole moment functions depending on the distance between atoms. Real molecules, however, are more complex systems and the vibrations possess anharmonic features. The analytical forms used to describe their motion have to be chosen taking into account molecular chemical properties and geometry.

Harmonic oscillators have selection rules $\Delta\nu=\pm 1$ with a fundamental vibrational band $\nu=1\leftrightarrow 0$ and hot bands (transitions between excited levels) $\nu_{i+1}\leftrightarrow\nu_i$ with $\nu_i\neq 0$.

Molecules which posses anharmonic oscillations have overtone transitions with selection rules $\Delta\nu=\pm 2,\pm 3,...$ are allowed but generally much weaker than fundamental transitions.

The harmonic oscillator model presents fundamental modes and also a combination of them $(\nu_i+\nu_j)$ with $i\neq j$. The combination transitions rely on anharmonic effects.

A molecule shows pure strong rotational transitions if it possesses a permanent dipole moment; vibrational transitions, instead, require a change in dipole. The dipole moment describes the polarity of a system of electric charges [3]:

$$\vec{\mu}=q\vec{r}_i, \tag{2.2.2}$$

where q is the charge and r_i is the charge separation.

Polyatomic molecule dipole moments can be expressed using analytical functions. An example of a functional form for one mode in a diatomic molecule is:

$$\mu\left(r_i\right)=\mu_e+\frac{d\mu}{dr_i}\,|_{r_e}\,\left(r_i-r_e\right)+\frac{1}{2}\frac{d^2\mu}{dr^2}\,|_{r_e}\,\left(r_i-r_e\right)^2+\cdots, \tag{2.2.3}$$

where μ_e is the permanent dipole moment and the other terms express the higher order dependency with internuclear separation. Molecules can have

- $\mu_e = 0$ **and** $\dfrac{d\mu}{dr_i} = 0$ Dipole moment is zero and molecules do not show IR transitions (for example homonuclear diatomic molecules).
- $\mu_e = 0$ **and** $\dfrac{d\mu}{dr_i} \neq 0$ Molecules show ro-vibrational transitions but no pure rotational spectra.
- $\mu_e \neq 0$ **and** $\dfrac{d\mu}{dr_i} \neq 0$ Molecules have ro-vibrational and pure rotational transitions.

2.2.2 Rotational Frequencies

Molecular rotation can be described by considering a reference system (x, y, z) with the centre of mass at the origin and its moment of inertia about the axes

$$I_p = \sum_i m_i r_{ip}^2, \tag{2.2.4}$$

where $p = x, y$ or z, m_i is the atom's mass and r_{ip} the distance from the axes p.

Molecules can be classified in terms of their inertia as

- **Linear molecules** $I_x = I_y, I_z = 0$.
- **Spherical Top** $I_x = I_y = I_z$.
- **Symmetric Top** $I_x = I_y \neq I_z$.
- **Asymmetric Top** $I_x \neq I_y \neq I_z$.

Within the rigid rotor approximation the rotational energy levels of a closed shell linear molecule is given by

$$E_{rot} = BJ(J+1), \tag{2.2.5}$$

where B is the rotational constant measured in MHz and J is the rotational quantum number $0, 1, 2, 3$.....

Selection rules are $\Delta J = 0, \pm 1$ or labelled as Q P R branches when associated with vibrational transitions. Vibrational perpendicular bands present P and R branches and parallel band PQR. More degenerate vibrational modes (bending modes of a linear molecule for example) possess a vibrational angular momentum $\vec{l}$ and the spectrum shows an l-doubling effect due to the coupling between vibrational and rotational quantum number:

$$\vec{J}_{TOT} = \vec{J}_{Rot} + \vec{l}, \tag{2.2.6}$$

with $\mid l \mid = \nu, \nu - 2, ...1$ or 0 for a degenerate bending frequency ν.

2.3 Symmetry Properties

$^{12}C_3$ possess a centre of symmetry and is formed by three symmetrically equivalent Boson nuclei. A consequence of this is ‟missing ″lines in the observed spectra. To understand this particular behaviour, we should briefly look at the symmetry properties and statistics of the C_3 system.

Using the Born-Oppenheimer approximation and separating vibrational and rotational motion we can see that the complete wave-function ψ_{TOT} is a product of the electronic ψ_e, vibrational ψ_v, rotational ψ_r and nuclear spin ψ_n:

$$\psi_{TOT} = \psi_e \psi_v \psi_r \psi_n. \tag{2.3.1}$$

The total wave function must be symmetric because carbon atoms follow Bose-Einstein statistics. The ground electronic wave-function is symmetric

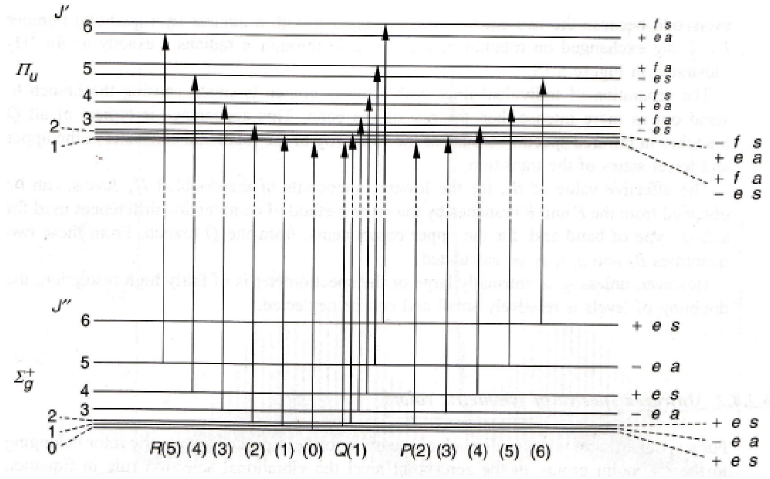

Figure 2.3: Vibrational and rotational energy levels including l-doubling effect for a transition between vibrational modes labelled following the molecular symmetries rules [13].

as is the nuclear one; it follows that the product between rotational and vibrational part must be symmetric too.

Because vibrational and rotational wave functions are both symmetric, the spectra ‟misses ″the lines that arise from states associated with an antisymmetric rotational-vibrational wave-function.

An example is shown in Figure 2.3. This shows the ro-vibrational transitions between the ground vibronic state and the fundamental bending band with

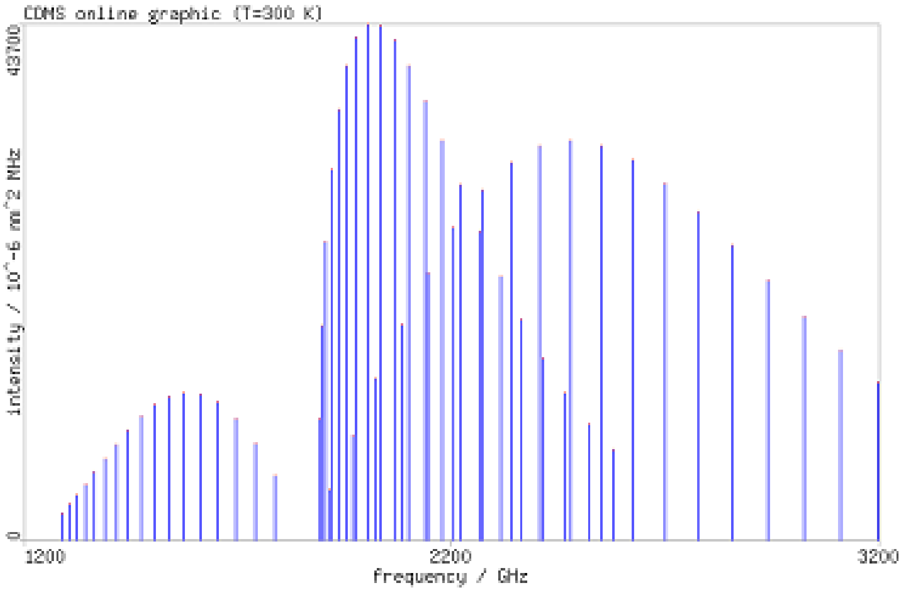

Figure 2.4: Fundamental bending mode of C_3 at 63.4166 cm^{-1}. Spectrum by R.Gendriesh et al. 2003, Z. Naturforsch. 58a,129.

the vibrational angular momentum $l = 1$ and where just the lines with $J =$ even are observable.

The parameter l describes the vibration angular moment which increases when the molecule is more bent.

The low fundamental bending frequency (i.e. extreme floppiness) of C$_3$, results in a very large l-doubling. In the linear configuration, degeneracy in l is observed. As the molecule becomes more and more like an asymmetric top this degeneracy is increasingly broken.

In conclusion, although C_3 is a linear molecule, it is possible to treat it as a special case of an asymmetric top and the *l*-doubling can be handled like the *k*-doubling (this is the doubling caused by the projection k of the molecular angular moment J along the rotation axis) in an asymmetric top. This means that calculations can be carried out using computer programs written for the calculation of the vibration-rotation spectra of non-linear triatomic molecules provided this program treats the transition from non-linear to linear geometry correctly.

2.4 Linear or Quasilinear Equilibrium Geometry?

An interesting problem for C_3 is determining its equilibrium geometry structure.

Molecules can show a linear, nonlinear or quasilinear geometry at the equilibrium configuration. The first two are self-explanatory. A molecule with quasilinear structure has a bent equilibrium structure but vibrates through the linear configuration even in its vibrational ground state [14].

For C_3, early CI-SDQ calculations (a method using Configuration of Iteration with single, double and quadruple excitation) performed by Kramer *et al.* [15] predicted a slightly bent equilibrium geometry with an equilibrium angle of $161.6\,^\circ$ and an effective bending potential that shows a linear configuration in state $(\mathrm{v}_1, \mathrm{v}_3 = 0)$ and $(\mathrm{v}_1 = 0,\ \mathrm{v}_3)$ (as result of strong bend-stretching coupling).

Molecules with "floppy" large amplitude vibration may present a large *l*-type doubling indicating a strong rotation-vibration coupling. As a consequence, they present fascinating features such as:

- Barriers to linearity due to the unusual low bending frequency that coupled with the symmetric and antisymmetric modes constrain the molecule to not easily reach the linear configuration.

- Mixing, inversion and splitting (resolving) of degenerate levels of the same J-rotational quantum number and different values of l; The l-doubling effect splits the rotational level J in two levels f and e (or $-$ and $+$ parity levels) with usually e levels lower in energy than the f. But it has been observed that in C_3 these levels could show as already said mixing and inversion features due to extrem floppyness in the bending mode.

- Anarmonicity and the presence of overtones.

Bunker [14] introduced a semi-empirical numerical method "Semi-rigid Bender Analysis" to determine the structural configuration of a molecule by analysing the shape of the electronic Potential Energy Surface. Also it has been found that the energy level splitting behaviour can be a good structure indicator.

Experimental studies due to Nortrup and Rolphing [16, 17] analyse respectively the bent-symmetric-stretch $(\mathrm{v}_1, \mathrm{v}_2, 0)$ and the bend-antisymmetric-stretch $(0, \mathrm{v}_2, \mathrm{v}_3)$ combination levels.

A Semi-rigid Bender Analysis also performed by Nortrup and Rolphing [18] demonstrated a linear equilibrium geometry. They analysed the $J = 2$ splitting between $l = 0e$ and $l = 2e$ (sigma-delta splitting). They show that the experimental splitting decreases as v_2 increases. Also in v_1 states the σ $(l = 0)$ and δ $(l = 2)$ state are inverted.

Nortrup and Rolphing therefore propose that a potential that exhibits a barrier to linearity cannot reproduce the small splitting (*i.e.*the low bending vibrational frequency). They therefore conclude that C_3 is linear.

Jensen reported that the l-splitting in the rotational structure of a given vibrational level is extremely sensitive to details of the potential surface [16]. In fact, the Potential Energy Surface chosen in this work to study C_3 [19] (from now on labelled AHM PES) shows an l-splitting that is too small in comparison with the experimental results. The AHM PES bending curve for the ground electronic level $X^1\Sigma_g$ and for the first exited electronic state A^1 is shown in Figure 2.5. These bending curves are obtained fixing the values for the bond-length coordinates and plotting the potential energy variation with the angle θ. As seen in the Figure, the first exited electronic state (at about 24000 cm^{-1}) presents a more complex structure characterized by the degeneration removal of the following molecular symmetries configurations (Π_u, Σ_u, Δ_u, Π_g) (respectively the blue, the purple, the black and the red curves). However, the purpose of this project is calculating the line list of C_3 molecule in its ground electronic state and this is the reason why we are interesting just in the green curve $X^1\Sigma_g$ of the Figure 2.5. The flatness of this potential curve is clearly evident; the green curve remains close to the zero-energy level up to about 130 degree and raises steeply after this value until it reaches wavelength of 12.500 cm^{-1}. This is a clear indication of the low bending frequency and the extreme floppiness of this molecule. At the cyclic geometry (theta equal to 60 degree) the C_3 molecule presents a conical intersection where the ground electronic state and the first exited electronic state with symmetry Δ_u show the same wavelength value of 12.500 cm^{-1} Figure 2.5.

In this thesis we agree that the C_3 molecule could have a linear geometry at equilibrium but the antisymmetric motion could experience a certain barrier to the linearity and vibrate through a bent configuration.

2.5 Experimental Research Into the Properties of C_3

Experimental research by Northrup and Sears [20, 16]; Northrup, Sears and Rohlfing [18]; Rohlfing and Goldsmith *et al.* [21, 17] show no barrier to linearity in the quite flat bending potential for either the zero point ($\nu_1 = \nu_3 = 0$) or the equilibrium stretching mode states of the C_3 molecule.

By contrast, they see that the molecule develops a barrier (of about 21 cm^{-1} and a bond angle of 162.5 °) in the linear configuration as the anti-symmetric stretch is excited. Moreover, they observed a strong bend-stretch interaction in the ground state. This is very unusual for linear molecules where the rotational constant of the antisymmetric stretching should decrease as the vibrational excitation increases.

An opposite trend is more usually observed where the molecule becomes more rigidly linear upon symmetric-stretch and more floppy when anti-symmetrically stretched.

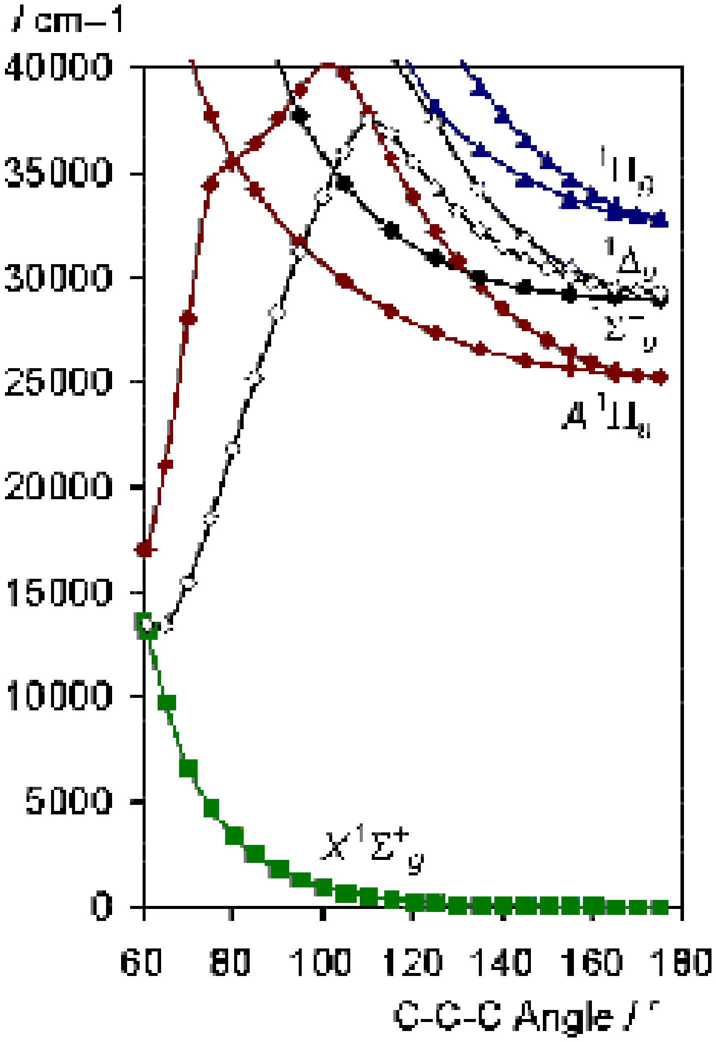

Figure 2.5: Potential energy surfaces for the ground electronic state X (green curve) and for the complex first exited electronic state A in D_{2h} molecular symmetries (Π_u, Σ_u, Δ_u, Π_g) as calculated by Ahmed *et al.* [19]

The experimental research of Northrup *et al.*suggests that the dramatic rise in the rotational constant as a function of the anti-symmetric stretching is correlated with the increasingly larger barrier to linearity in the effective bending potential. They suggest that "the shape of the potential is fairly insensitive to small changes in the bond length or with its variation with the bending angle and the dependence of the bond length on the bending angle is relevant " [16].

The type of absorption bands observed depend upon the direction in the rotating molecule of the oscillating electric dipole moment induced by the electromagnetic radiation (as discussed by Duxbury *et al.* [2]). In the symmetric stretching motion, there is no variation in the transition dipole moment; that means that it can be observed using Raman spectroscopy but not in IR. Raman spectroscopy techniques give information about ro-vibrational features using scattering light from the molecular system. This reveals information not displayed by IR spectroscopy.

The anti-symmetric stretching and bending fundamentals are Far Infrared and Infrared active and they show PR (selection rules $\Delta J = +1$ (P branch) and $\Delta J = -1$ (R branch)) and PQR (selection rules $\Delta J = 0$ (Q branch)) types of absorption bands respectively. The Q branch in the bending motion can be observed because a vibrational change can happen without simultaneous rotational transitions.

Early theoretical studies by Kramer *et al.* [15] show a very high transition dipole moment for the ν_3 band in comparison with the one for ν_2 band. Recent laboratory experiments by Schmuttenmaer *et al.* [22] and theoretical studies performed by Jensen *et al.* [23] disagree with Kramer's theory and in fact show a similar fractional absorption for the two IR-active bands.

2.6 Summary

In summary the C_3 molecule has the following properties:

Linearity of Structure It has a linear or quasi-linear structure in its ground electronic state.

Symmetry of Structure It has a centre-symmetric structure *i.e.*it possesses a centre of inversion.

Dipole Moment It does not have a permanent dipole moment; this means that strong pure rotational transitions cannot be observed.

π_g **Electrons** π_g electrons are electrons in overlapping p-orbitals.

The bending frequency of a molecule is therefore related to the π_g electrons as they act like a "backbone" [24]. The C_3 molecule does not possess any of these type of electrons and this leads to

Low Bending Frequency An unusually low bending wavenumber of 63.4165 cm^{-1} (see Walsh [25]).

Potential Energy It has a relatively flat potential energy surface. This means that at low frequencies it is already possible to observe great vibrational displacements.

Floppiness Due to the low bending frequency the C_3 molecule presents a high degree of floppiness. Indeed, in the first exited state, where π_g orbital is occupied, the fundamental bending wavenumber go up at about 350 cm^{-1} [24].

2.6.1 Use of Molecular Properties For Astronomical Observations

C_3 was observed for the first time in astrphysical contexts by Higgins *et al.* [26] in emission from comets in 1882 and later by Hinkle [27] in absorption through its fundamental antisymmetric stretch band (ν_3) in the atmosphere of the cool carbon star IRC +10216. This object is a carbon rich Mira variable with an unusually thick and dense dust molecular envelope. For this reason it gives a natural laboratory to understand the interstellar and circumstellar chemistry (see Cernicharo and Goicoechea [28]).

In 2000, observations made by Cernicharo *et al.* [28] showed the detection at the low bending frequency, again in IRC +10216 and in a massive dense molecular cloud: Sagittarius B2 which is the richest concentration of molecules in the Milky Way. The detection of this unusual and quite low fundamental bending band opened new possibilities to detect other molecular species without a permanent dipole moment [12], *i.e.*lacking pure rotational transitions.

Most recently Harris *et al.*detected the fundamental antisymmetric-stretch band ν_3 in the outer atmosphere of the cool AGB (Asymptotic giant branch) carbon star WZ Cas [29].

Chapter 3

Variational Approach to the Study of Triatomic Molecules

An already tested and successful approach to study the infrared spectra of molecules is the separation of the electronic problem from the nuclear one using Born-Oppenheimer's approximation. This approximation is based on the fact that electrons are a thousand times less massive than nuclei which allows setting the nuclear kinetic energy to zero in electronic structure calculations.

As described by Jensen and Bunker [30] there are two ways of solving the bound state nuclear motion problem which arises as the second step in the BO approximation: the perturbation theory approach and the variation theory approach. The perturbational approach is based on studying a complex system approximating it to a simple one and finds an approximate solution to the Schrodinger equation. Despite being useful for studying several systems, it is not well suited to describing a molecule with large amplitude motions such as C_3. A variational approach is more suitable for studying C_3 characteristics and a description of this method will be given in the next section.

3.1 Quantum mechanics theory

Schrödinger's equation is used in quantum mechanics to determine allowed quantum states for microscopic and macroscopic systems. The time-independent equation states that:

$$H\Psi = E\Psi, \tag{3.1.1}$$

where H is the Hamiltonian Operator, Ψ is the wavefunction of the particle, and E is the energy of the particle.

The Hamiltonian operator H of any system is given by the sum of its kinetic and potential energy. For C_3, working in Jacobi coordinates, the operator is written [31]

$$H(r_1, r_2) = K_v^1 + K_{vr}^1 + \delta_{k',k}\langle j'k'|V(r_1, r_2, \theta)|jk\rangle_\theta, \tag{3.1.2}$$

where K_v and K_{vr} are respectively the vibrational and the ro-vibrational kinetic energy operators, $V(r_1, r_2, \theta)$ is the potential energy function and $\langle j'k'|$ and $|jk\rangle$ the eigenstates for the ro-vibrational transitions with quantum number j and k. δ is the delta function (it takes the value zero for all $k \neq k'$).

Vibrational motions and their characteristic frequencies are determined using analytical functions known as Potential Energy Surfaces (PES) describing electronic energy interactions between atoms making up a bonded chemical system.

- **Radial basis** Symmetric and antisymmetric motions can be approximated using Morse-like functions [1] with eigenfunction:

  $$\mid n >= H_n(r) = \beta^{\frac{1}{2}} N_{n\alpha} exp(-\frac{y}{2}) y^{\frac{(\alpha+1)}{2}} L_n^\alpha(y), \tag{3.1.3}$$

  with

  $$y = Aexp[-\beta(r - r_e)], \tag{3.1.4}$$

where

$$A = \frac{4D_e}{\omega_e}, \beta = \omega_e(\frac{\mu}{4D_e})^{\frac{1}{2}}, \tag{3.1.5}$$

where r_e is the equilibrium distance, μ is the reduced mass, ω_e is the fundamental frequency, D_e is the dissociation energy and $N_{n\alpha}L_n^{\alpha}(y)$ normalized generalized Leguerre Polynomials with α equal to A rounded.

- **Angular basis** These are Legendre polynomials:

$$P_n(x) = \frac{1}{2^n n!}\frac{d^n}{dx^n}[(x^2-1)^n], \tag{3.1.6}$$

The potential energy surface (PES) $V(r_1, r_2, \theta)$ necessary to perform nuclear motion calculations can be constructed by estimating the electronic energy for each nuclear geometric configuration (using a program such as MORPLO [32] for example). The quality of the PES sets the accuracy of the subsequent ro-vibrational calculations. For this reason, much experimental and theoretical effort has been focused on determining the right shape of the potential-energy function [23]. It is observed that the most accurate PESs are computed using ab-initio starting points, with the resulting surface being empirically adjusted to improve the agreement between the computed energies and experimental data [33].

Having constructed the PES the bound states of the system can be determined using a basis set of square integrable eigenfunctions (within Hilbert space) expressed in a one-dimensional array form and the Hamiltonian H in a matrix form. The equation can be solved by diagonalizing the H-matrix and obtaining eigenvalues representing energy levels of the system. Increasing the set of functions forming the H-matrix, the eigenvalues will converge more and more to their exact value.

Highly floppy molecular motion is better described using a Discrete Variable Representation (DVR) matrix [31] obtained by performing an orthogonal transformation in which the basis function set is represented in a coordinate space rather than in a functional space. Successive diagonalizations and truncations lead to a reduction in the dimension of the analytical problem and computational time [31].

3.1.1 Computational Solution

A program has been written by Tennyson *et al.* [1] for performing nuclear motion calculations using variational techniques (this is referred to as the DVR3D program suite). It requires as input a PES and preliminary tests are necessary in order to determine if they are appropriate to carry out the calculations or if they need some adjustments.

DVR3D uses variational techniques, where the wave-functions Ψ are defined by a complete set of weighted, orthogonal grid points expressed in Jacobi coordinates. The program uses Legendre polynomials as angular basis functions and either Morse oscillator-like functions or spherical oscillator as radial basis functions.

In the case of C_3, the linear equilibrium geometry encourages the use of Jacobi coordinates R, r and α (see Figure 2.1) and Morse oscillator-like functions. These functions are defined in terms of parameters that must be optimized in order to achieve a balance between computer power, time expense and the convergence of all the energy levels (the aim for this work is 0.01 cm^{-1} spectroscopic accuracy).

Due to the nuclear spin statistic of C_3, some rotation-vibration symmetry blocks are ‟missed ″. This means for J even just ee (even-vibrational/even-rotational wave-function) and oo symmetry will be considered, and for J odd just the eo and oe blocks.

DVR3D allows not just bound rotation-vibration energy level calculations but also wave-functions, expectation values and if a Dipole Moment Surface is supplied, Einstein coefficients and temperature-dependent spectra. The calculations to obtain an accurate infrared line-list can be very expensive in terms of computer power and time, and test procedures are necessary to evaluate the quality and goodness of the PESs and DMSs inputted into the DVR3D program.

3.2 Potential Energy Surface

Recently, three-dimensional Potential Energy Surfaces for the carbon trimer have been constructed by fitting some ab-initio points calculated using the MOLPRO suite [32] program (see Mladenovic *et al.*. [34] (MLAD), Jensen *et al.* [23] and Ahmed *et al.* [19] (AHM1)Figure 2.5).

Jensen's Potential energy surface is too bent to reproduce the l-doubling sigma-delta splitting and it will not be used to perform test calculations with DVR3D. The other two potential surfaces MLAD and AHM will be analysed and tested. Both surfaces V have the following functional form:

$$V = \sum_{i,j,k} C_{i,j,k} X_1^i X_2^j \theta^k \tag{3.2.1}$$

where $X_1 = \mathrm{q}_1 + \mathrm{q}_2 - 2$ and $X_2 = \mathrm{q}_1 - \mathrm{q}_2$ are the symmetric and antisymmetric stretch coordinates respectively, θ is the bond-angle and $C_{i,j,k}$ are parameters obtained by MLAD and AHM by fitting the ab-initio points to calculate the C_3 PES.

A large basis set has allowed the MLAD PES to reproduce energy levels up to 300 cm^{-1}, above the zero-point energy, with good agreement (a standard deviation of 7.3 cm^{-1}) with experiments.

The AHM1 pure ab-initio PES is not as accurate as MLAD's (it has an average error of 61.6cm^{-1}). Adjustments by a fitting of a few potential coefficients to the available experimental data enables the AHM1 Potential to give vibrational levels up to 8000cm^{-1} with a standard deviation of 2.8 cm^{-1} from the experimental data. A comparison between the two PESs is given in Figure 3.1.

3.2.1 Energy Level Calculations Using the Mladenovic *et al.*. and Ahmed *et al.*. PES

The ro-vibrational energy level calculation with $J = 0$ obtained using MLAD and AHM1 PESs as input to the DVR3D program suite are shown in Table 3.1.

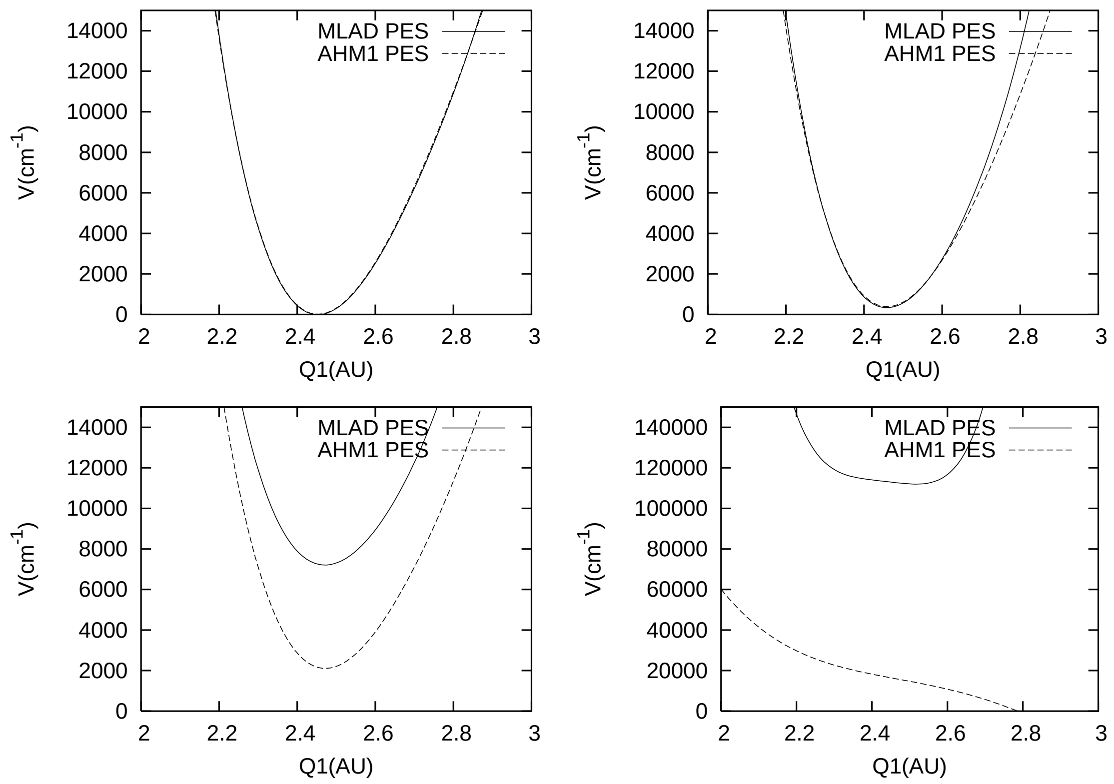

Figure 3.1: MLAD and AHM1 PESs as a function of the bond length q_1. q_2 is fixed at the equilibrium values and θ from the left top assumes the value $10\,^\circ$, $60\,^\circ$, $90\,^\circ$, $120\,^\circ$ respectively.

Table 3.1: Differences, in cm^{-1}, between the experimental [20, 21, 16, 17, 18, 35, 22, 36] and calculated vibrational energy levels. Calculations performed by Mladenovic [34] and Ahmed *et al.* [19] are compared with our DVR3D calculations obtained respectively using the MLAD and AHM PES's.

			Observed	Obs−calc			
ν_1	ν_2	ν_3	G(ν)	[34]	MLAD	[19]	AHM
0	2	0	132.80	0.5	5.7	2.5	2.5

Continued on Next Page. . .

			Observed	Obs−calc			
ν_1	ν_2	ν_3	G(ν)	[34]	MLAD	[19]	AHM
0	4	0	286.11	-2.7	-1.9	-0.7	-0.6
0	6	0	461.09	-11.0	-20.1	0.7	0.7
0	8	0	647.59	-15.1	-56.4	-1.2	-1.2
0	10	0	848.40	-19.1		-2.0	-2.1
1	0	0	1224.20	-5.3	1.9	5.2	5.1
1	2	0	1404.10	-1.0	7.3	1.8	-1.5
1	4	0	1590.05	0.1	3.4	0.1	0.1
0	18	0	1773.37			-0.1	-1.8
1	8	0	1990.52	-6.6	-43.6	-3.4	-3.5
0	0	1	2040.02	0.6	3.3	2.0	2.0
0	2	1	2133.89	4.7	-3.0	0.1	0.1
1	10	0	2210.50	-15.3		-0.7	-0.9
2	0	0	2435.20	-10.5	5.4	2.5	2.4
1	12	0	2439.90			1.4	1.0
0	24	0	2575.92			-0.4	1.0
2	2	0	2656.33	-3.9	-15.3	0.4	0.3
2	4	0	2876.90	-0.4	6.9	1.9	1.8
2	6	0	3099.90	-1.6	-3.6	3.3	3.1
1	0	1	3259.90			1.2	1.1
3	0	0	3636.10			0.1	-0.1
3	2	0	3894.30			-0.1	-0.4
0	0	2	4035.37			0.4	0.1
0	2	2	4110.89			2.4	2.2
3	4	0	4146.30			2.5	2.2
0	4	2	4211.33			3.9	3.6
0	6	2	4339.42			5.1	4.6
3	6	0	4392.78			2.4	2.0
2	0	1	4459.30			-0.8	-1.2
3	8	0	4641.03			2.9	2.4
0	10	2	4651.60			3.4	2.3
0	12	2	4832.50			3.4	2.0
4	0	0	4828.70			-1.3	-1.9
0	14	2	5029.00			4.4	-2.1
0	16	2	5236.60			4.1	-2.0

Continued on Next Page...

ν_1	ν_2	ν_3	Observed G(ν)	Obs−calc [34]	MLAD	[19]	AHM
1	0	2	5265.40			-7.7	-8.3
1	2	2	5367.20			-7.1	-8.0
1	4	2	5495.40			-5.6	-6.4
1	6	2	5643.50			-4.1	-5.1
1	8	2	5809.10			-2.4	-4.0
5	0	0	6013.60			-1.7	-3.1
6	0	0	7191.30			-0.9	-4.8
7	0	0	8361.50			0.3	-6.4

The calculations were performed up to energy levels of 12500 cm^{-1}(Ahmed [19]) where a conical intersection with an electronic exited state PES forbid further calculations using the present method.

To reproduce accurate spectra of cool star atmospheres in the temperature range of 2000 − 4000 K it is necessary to perform calculations with a high rotational quantum number. Considering that the calculated and observed rotational constant is about 0.4cm^{-1} at an energy of 12000 cm^{-1}, J should be approximately 86 (from equation 2.2.4). For this reason, energy levels with $J \gg 0$ have been tested. See Tables 3.1 for the MLAD and AHM1 PES and comparison with experimental data. Both potential surfaces will need some adjustments and probably a fit with experimental data could increase the accuracy of the results.

3.2.2 Testing Procedure and Unexpected Levels

As we already said, a potential energy surface represents the electronic potential energy field of a chemically bonded system for each geometric configuration of the carbon nuclei.

This surface needs to cover the whole range of nuclear configurations without regions or points in which the value of the energy is unreliable.

During the testing procedure to optimize DVR3D parameters, the AHM PES presented an unexpected and unreasonable behaviour. In particular, when varying the values of the scattering coordinates R and r over certain values, unexpected lines are found to appear.

As we have already seen, the AHM potential energy surface is given in symmetric and antisymmetric stretch coordinates X_1, X_2 and θ. A transformation is therefore necessary to transform into Jacobi coordinates r, R and α (the coordinate system used in the DVR3D program).

A subroutine written in Fortran performs the transformation between the

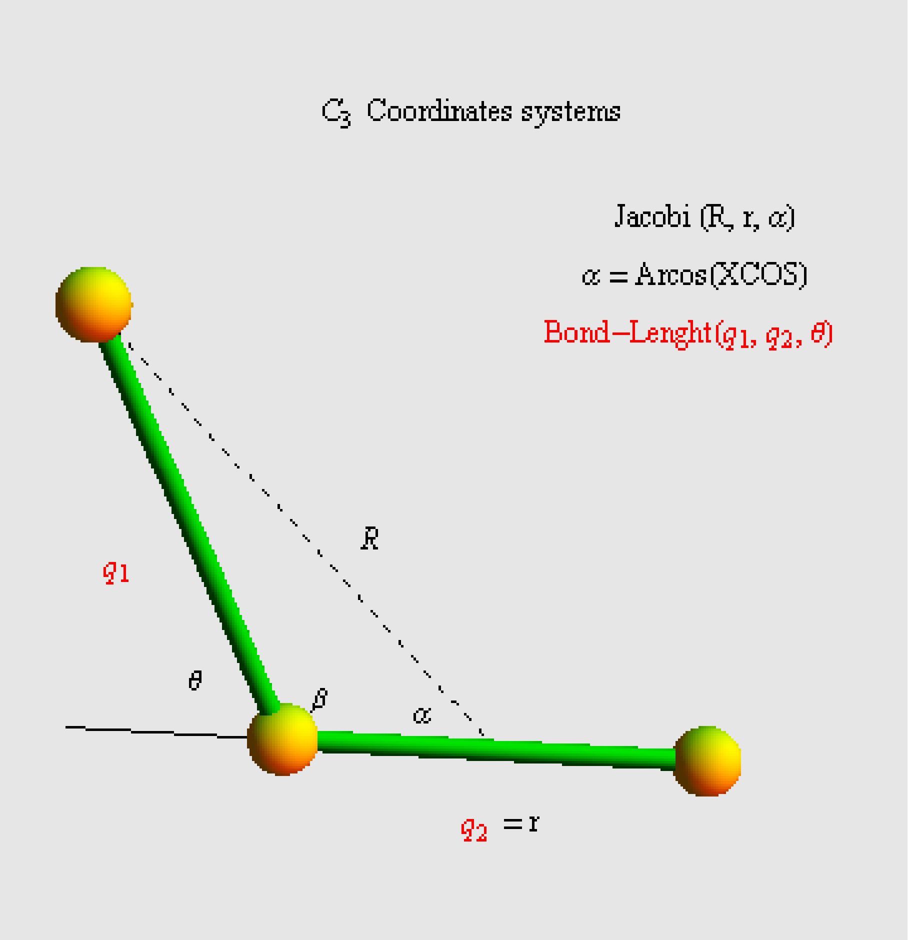

Figure 3.2: C_3 coordinate systems: Bond-Length and Jacobi

Bond-Length coordinates (q_1, q_2 and θ) and the Jacobi coordinates (R, r, XCOS =cos(α)) using following relationships:

$$
\begin{aligned}
YY &= \left(\frac{\mathrm{q}_2}{2}\right) && (3.2.2)\\
R &= r\left(\sqrt{\mathrm{q}_1^2 - \mathrm{q}_2}\cos(\beta)\mathrm{q}_1 + \frac{\mathrm{q}_2^2}{4}\right) && (3.2.3)\\
r &= \mathrm{q}_2 && (3.2.4)\\
XCOS &= \frac{\frac{\mathrm{q}_2^2}{2} - \mathrm{q}_1\mathrm{q}_2\cos(\beta)}{\mathrm{q}_2\sqrt{\mathrm{q}_1^2 - \mathrm{q}_2\cos(\beta)\mathrm{q}_1 + \frac{\mathrm{q}_2^2}{4}}} && (3.2.5)
\end{aligned}
$$

It seemed that over certain values the PES presented holes that are points (or molecular configurations) for which it does not give reliable energy values.

It was necessary to make some adjustments to the AHM PES in order to use it within DVR3D. To calculate where the PES stopped working properly it was first necessary to perform a coordinate transformation into Jacobi coordinates in order to have a comparable reference to AHM PES features (expressed in bond-length). Deriving the expressions for (q_1, q_2 and θ) from equation (3.1.2) it is possible to rewrite the PES in Jacobi coordinates as follows (from equation 3.1.1)

$$V = \sum_{i,j,k} C_{i,j,k} J_1^i J_2^j J_3^k \tag{3.2.6}$$

where

$$J_1 = r_1 - 2r_e + \sqrt{\frac{{r_1}^2}{4} - r_2\cos(\alpha)r_1 + {r_2}^2}, \tag{3.2.7}$$

$$J_2 = \sqrt{\frac{{r_1}^2}{4} - r_2\cos(\alpha)r_1 + {r_2}^2} - r_1, \tag{3.2.8}$$

$$J_3 = \cos^{-1}\left(\frac{r_1 r_2 \cos(\alpha) - \frac{{r_1}^2}{2}}{r_1\sqrt{\frac{{r_1}^2}{4} - r_2\cos(\alpha) r_1 + {r_2}^2}}\right), \tag{3.2.9}$$

C_3 has a conical intersection at 12500 cm^{-1} (Vlim) as shown already in Figure 2.5, this is because at the equilateral triangle configuration the ground state potential energy surface overlaps with an exited state surface; this means that the energy level calculations should be stopped at V=Vlim including a constraint for the AHM PES expression. Introducing deformation coordinates makes it easy to find out which conditions need to be added in order to constrain the PES to the region of interest. Deformation coordinates are defined as

$$\mathrm{S}_1 = \frac{\mathrm{Q}_1 + \mathrm{Q}_2 + \mathrm{Q}_3 - 3\mathrm{r}}{\sqrt{3}}, \tag{3.2.10}$$

$$\begin{aligned}
\mathrm{S}_2 &= \frac{\mathrm{Q}_2 - \mathrm{Q}_1}{\sqrt{2}}, && (3.2.11)\\
\mathrm{S}_3 &= \frac{-\mathrm{Q}_1 - \mathrm{Q}_2 + 2\mathrm{Q}_3}{\sqrt{6}}, && (3.2.12)\\
\tan\phi &= \frac{\mathrm{S}_1}{\mathrm{S}_2}, && (3.2.13)\\
&= \sqrt{3}\frac{\mathrm{Q}_2 - \mathrm{Q}_1}{-\mathrm{Q}_1 - \mathrm{Q}_2 + 2\mathrm{Q}_3}, && (3.2.14)\\
\phi &= \tan^{-1}\left(\frac{\sqrt{3}(\mathrm{Q}_2 - \mathrm{Q}_1)}{-\mathrm{Q}_1 - \mathrm{Q}_2 + 2\mathrm{Q}_3}\right), && (3.2.15)\\
\mathrm{S} &= \sqrt{\frac{2}{3}}(\mathrm{Q}_1 + \mathrm{Q}_2 + \mathrm{Q}_3), && (3.2.16)\\
\mathrm{Q}_3 &= \sqrt{\mathrm{Q}_1^2 + 2\mathrm{Q}_2\cos(\theta)\mathrm{Q}_1 + \mathrm{Q}_2^2}. && (3.2.17)
\end{aligned}$$

Imposing equilateral configurations Q1=Q2=Q3 the above equations become

$$\mathrm{S}_1 = 3\frac{Q2 - \mathrm{r}}{\sqrt{3}}, \tag{3.2.18}$$

$$
\begin{aligned}
\mathrm{S}_2 &= 0, && (3.2.19)\\
\mathrm{S}_3 &= 0, && (3.2.20)\\
\mathrm{S} &= \sqrt{\frac{2}{3}}3\mathrm{Q}_2 = \sqrt{6}\mathrm{Q}_2, && (3.2.21)
\end{aligned}
$$

It was found that the conditions for $R < 2.6d0$ and $R < 2.0689d0 * (r - 1.55d0)$ correspond avoidance of the regions where the PES shows an incorrect behaviour (see Figure 3.3). The line

$$R = 2.0689d0 * (r - 1.55d0), \tag{3.2.22}$$

was traced so as to cut the surface at the point beyond which the hole appears. The coefficients of the line were found through an empirical search varying them until the correct cut was obtained. The constraint $\mathrm{S}_1 > 0.835703437d0$ is found from equation 3.1.24. This imposes the maximum value for Q calculated using the triangle rule with the fixed value $R = 2.6d0$.

All of these conditions need to be combined with the other constraint $xcos < 0.45d0$ corresponding to the value where DVR3D stops calculating values for each angular grid-point.

A program was written with `Mathematica`™to produce a visual representation of the PES behaviour and applying the corrections.

The `Mathematica`™program performs

- PES coordinate transformation from Bond-Length to Jacobi coordinates and plots (see Figure 3.3) representations of PES in Jacobi coordinates. This allows one to visualize the PES holes and the regions where critical values are encountered.
- contour plots of the surface (Figure 3.4) fixing the range for R and r and visualizing them together with the lines used to cut the PES, such as Equation 3.2.22.

The following lines were used in the Fortran subroutine to implement the constraints when running DVR3D to perform energy levels calculations:

$$\mathbf{IF}(\mathrm{S}_1 > 0.835703437d0 \wedge xcos < 0.45d0) \Rightarrow V = V_{\mathrm{Lim}} \quad (3.2.23)$$

$$\mathbf{IF}(R < 2.6d0 \wedge xcos < 0.45d0) \Rightarrow V = V_{\mathrm{Lim}} \quad (3.2.24)$$

$$\mathbf{IF}(R < 2.0689d0 * (r1 - 1.55d0) \wedge xcos < 0.45d0) \Rightarrow V = V_{\mathrm{Lim}} \quad (3.2.25)$$

Adding these constraints to the PES the problem of the appearance of unexpected lines was partially resolved as shown in Table 3.2.

Having constrained the PES to resolve the issue of unexpected lines in the spectra we must be aware that too many surface constraints could lead to problems in convergence. The issue of convergence is addressed in the next section.

3.2.3 Convergence Tests

Definition of Convergence

Convergence describes the tendency of a quantity towards a certain value and in this particular case sets the accuracy of energy level calculations.

The Energy level convergence needs to be achieved finding optimal value for the DVR3D parameters. A compromise between accuracy and computational time needs to be taken into consideration when radial and angular points are chosen in DVR3D and when the dimensions of the vibrational and rotational problem are set.

Testing Proceedure

Convergence tests for the pure vibrational problem were performed for $J = 0$. Parameters were chosen in order to perform a correct description of the molecular system using DVR3D as a computational theoretical tool. DVR3D requires as input a file with 9 lines in which all the settings can be specified [1].

Table 3.2: Vibrational energy levels calculations performed by Ahmed *et al.* [19] are compared with DVR3D calculations obtained respectively using the AHM and Corrected AHM PES's.

			Energy (cm^{-1})		
ν_1	ν_2	ν_3	AW04 [19]	AHM	Corr AHM
0	0	0	0	0	0
0	2	0	137.99	137.97	137.97
0	4	0	294.51	294.46	294.46
0	6	0	468.09	468.08	468.08
				653.73	
0	8	0	656.49	656.49	656.50
0	10	0	858.1	858.16	858.20
0	12	0	1072.06	1071.32	1072.27
				1073.17	
1	0	0	1226.7	1226.77	1226.77
0	14	0	1297.43	1296.70	1298.22
1	2	0	1410	1410.08	1410.08
				1483.92	
0	16	0	1533.97	1537.59	1535.07
1	4	0	1597.65	1597.66	1597.67
0	18	0	1781.17	1764.15	1775.14
1	6	0	1794.51	1794.59	1794.59
			1915.63		1978.3
1	8	0	2001.62	2001.73	2001.73
0	20	0	2038.79		
0	0	1	2045.72	2045.68	2045.69
				2079.16	
0	2	1	2141.49	2141.49	2141.49
				2158.80	
1	10	0	2218.9	2219.03	2219.07
				2235.25	
0	4	1		2268.92	2268.92
0	22	0	2306.43	2315.56	2411.92
0	6	1		2418.38	2418.40
2	0	0	2440.4	2440.514	2440.52
1	12	0	2446.2	2446.24	2446.63
				2472.79	
0	24	0		2584.02	2521.45

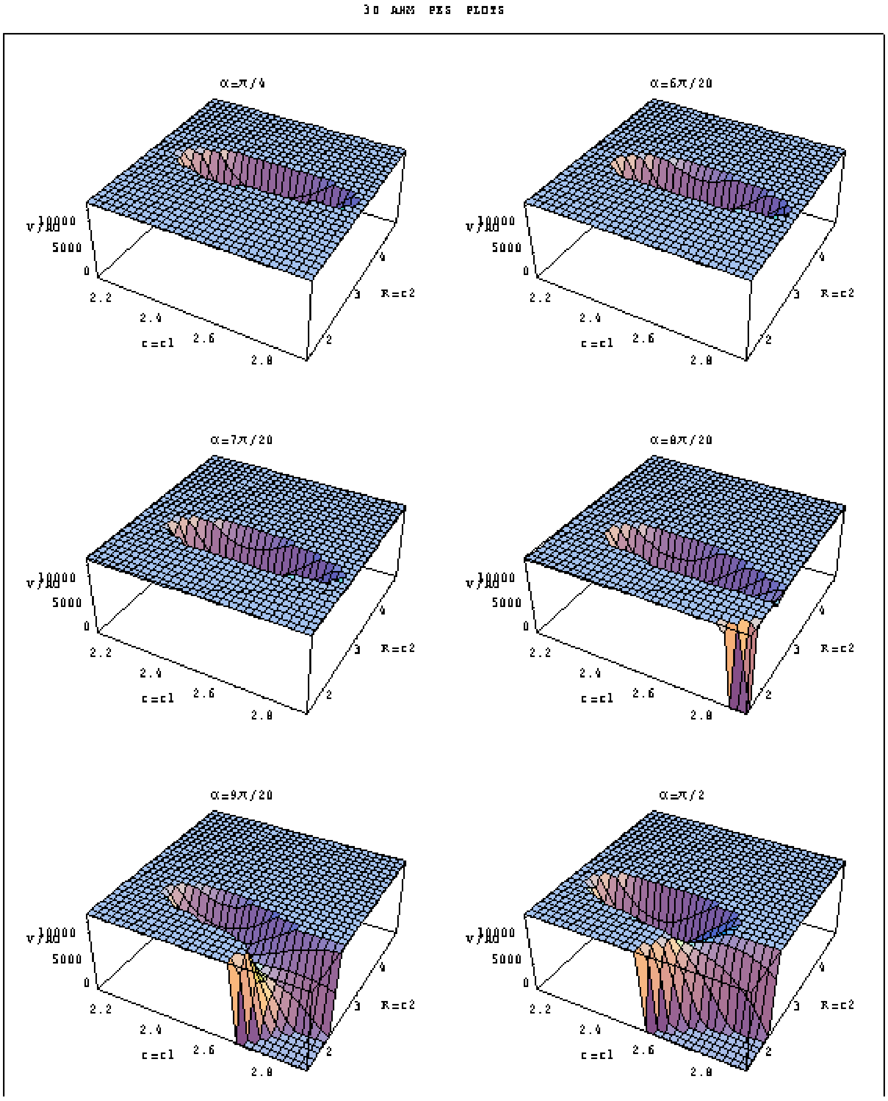

Figure 3.3: 3D Plots for AHM PES expressed in Jacobi coordinates fixing α values $(\pi/4, 6\pi/20, 7\pi/20, 8\pi/20, 9\pi/20, \pi/2)$)

- **NPNT1/NPNT2** number of DVR points in R/r from Gauss-(associated) Laguerre quadrature.
- **NALF** number of DVR points in θ from Gauss-(associated) Legendre quadrature.
- **MAX3D** maximum dimension of the final Hamiltonian.
- **EMAX2** is the second cut-off energy in cm^{-1} with the same energy zero as the potential.

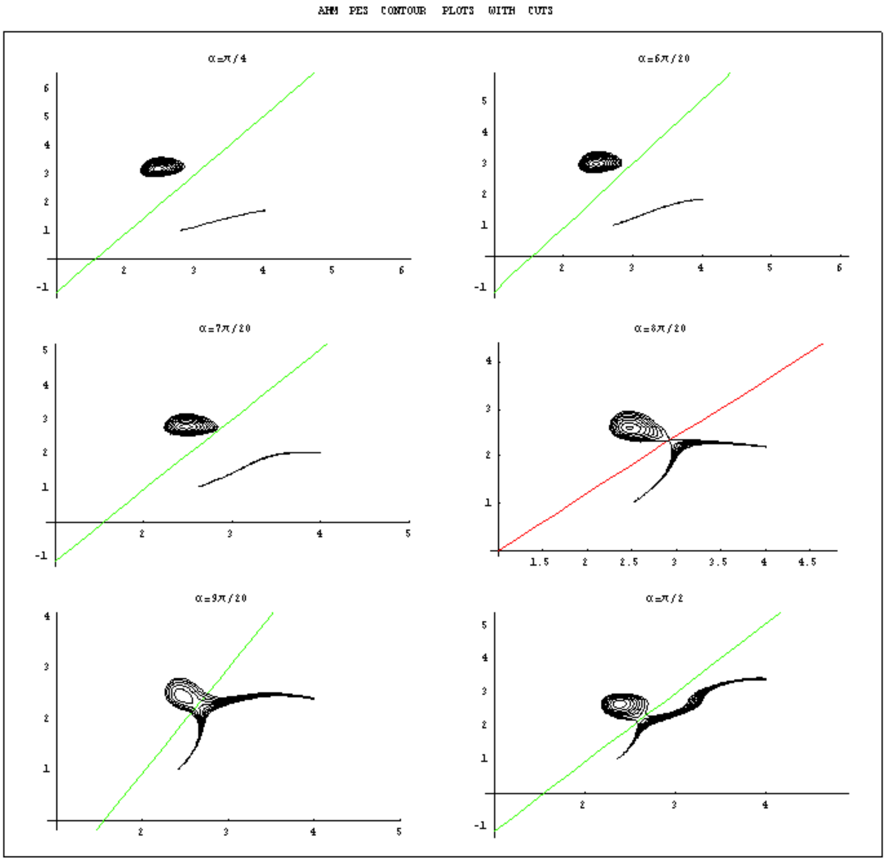

Figure 3.4: Contour plots in Jacobi coordinates fixing α values $(\pi/4, 6\pi/20, 7\pi/20, 8\pi/20, 9\pi/20, \pi/2)$ and line equation used to cut the potential energy surface to avoid holes.

- **ZCUT= True** final dimension selected using an energy cut-off given by EMAX2.
- **ZCUT= False** final dimension determined by MAX3D.

The number of radial and angular points and the Hamiltonian dimension were chosen. The initial values were set considering specific properties of the molecule and its PES, and then iteratively optimized.

First step Radial numbers (NPNT1, NPNT2) optimization.

- Morse oscillator parameter (r_e, ω_e, D_e) varied until the stability of energy levels results is demonstrated.
- fixing Morse parameters NPNT is varied until the energy level differences between previous and successive calculations are at the accuracy of order of 0.01 cm^{-1}.

Second step Number of angular functions (NALF) and Hamiltonian dimension optimization.

- Setting values for $ZCUT = False$, $NALF = 80$ and $MAX3D = 2000$ (these are set according to experience from previous calculations) the output at the calculation will give a value for the energy in wavenumber E^*.
- Test the energy level stability with values $ZCUT = True$, $NALF = 90$, $MAX3D = 3000$ and $Emax3D = E^*$.

Then optimal values for: r_e, we, De should be found for both radial and Jacobi coordinates.

Results

The final optimized values are:

- Radial number of points for $R = 56$, for $r = 26$ and the angle is $\alpha = 80$.
- Hamiltionian dimension is 2000.
- Morse oscillators optimized parameters expressed in a.u. are
  - $r_e = 3.675$, ${}_{e1} = 0.005$, De$_1 = 0.3$
  - $r_e = 2.585$, ${}_{e2} = 0.010$, De$_2 = 0.3$.

Issues and Futher Work

An important parameter to determine is the size of the Hamiltonian in the DVR3D rotation module ROTLEV3. This value called IBASS has to be determined empirically in order to reach energy level convergence. It was partially determined but further tests are necessary.

Tests were also done for several quantum numbers J. When looking at large J, a problem was encountered with the program used to perform the calculations.

Early test results for $J = 20$ shows that the possible value for IBASS has to be greater than 750. Further tests to find a value for IBASS are necessary with J at larger than at least 40.

3.3 Dipole Moment Surface

The second thing needed to calculate a line-list is a reliable Dipole Moment Surface (DMS).

3.3.1 Constuction of a DMS

As described for the PES, a DMS is built by interpolating ab-initio dipole moment components estimated for each nuclear geometric configuration using appropriate functional forms. The C_3 molecule has no permanent dipole moment but the displacements from equilibrium induce a dipole moment component.

Comparison of ab-initio and Fitted Dipole Moment Surfaces for C_3

If a working DMS is already available, one can compute transition intensities without performing ab-initio calculations and interpolation. In the case of C_3, ab-initio dipole moment calculations are already available. These were kindly provided by Colin Western, School of Chemistry, University of Bristol.

The 587 ab-initio points (for each component) were calculated by Ahmed at *et al.* [19] (AHM2) using the MRCI (Multi-Reference Configuration Iteration) method with the MORPLO Package [32].

Despite the availability of ab-initio dipole surfaces for C_3 previously constructed by Jorgensen *et al.*. [37] (JORG) and Jensen *et al.* [23] (JENS), we decide to built a new DMS due to the higher quality of AHM ab-initio calculations for the reason explained below.

3.3.2 The Jorgensen and Jensen DMS

The surfaces of Jorgensen [37] were obtained to an accuracy sufficient for the astrophysical predictions that their work required. It will not be tested here but these results have been compared with my calculations (see table 3.5 and 3.4). While Jorgensen placed less emphasis on describing the properties of the molecule near equilibrium geometry, Jensen *et al.*. [23] focused their study instead on the behaviour near the equilibrium configuration.

The JENS DMSs were tested and comparisons made to test the new DMS. The JENS DMS was constructed by fitting the p and q molecular dipole moment components (see Figure 3.5 where axes x and z represent p and q axes) for θ between 180 ° (linear) and 90 ° and bond lengths from 1.16 to 1.43 $\AA$. Dipole moments were calculated using the MOLECULE-SWEDEN code [38]. But JENS final fit shows insufficient numerical stability; for this reason, and because of the larger AHM ab-initio grid points range, we believe that the AHM MRCI ab-initio calculations should be used instead.

3.3.3 A New Formulation of the DMS

AHM's functions were calculated for θ between 180 ° (linear) and 60 ° (equilateral triangle geometry) and bond lengths ranging from 0.4 $\AA$ to 1.29497$\AA$.

AHM ab-initio points were fitted using a functional form proposed by Partridge and Schwenke(PS) [33] to study the water problem. It has been necessary to perform a coordinate transformation between the coordinate reference system used by AHM and the one used by Partridge. The carbon atoms are set in the xz plan with the central atom at the origin of the system and the remaining atoms having coordinates (atom 1) $x = q_1 \cos(\frac{\theta}{2})$, $z = q_1 \sin(\frac{\theta}{2})$ and (atom 2) $x = q_2 \cos(\frac{\theta}{2})$, $z = -q_2 \sin(\frac{\theta}{2})$. The coordinate system is shown in Figure 3.5.

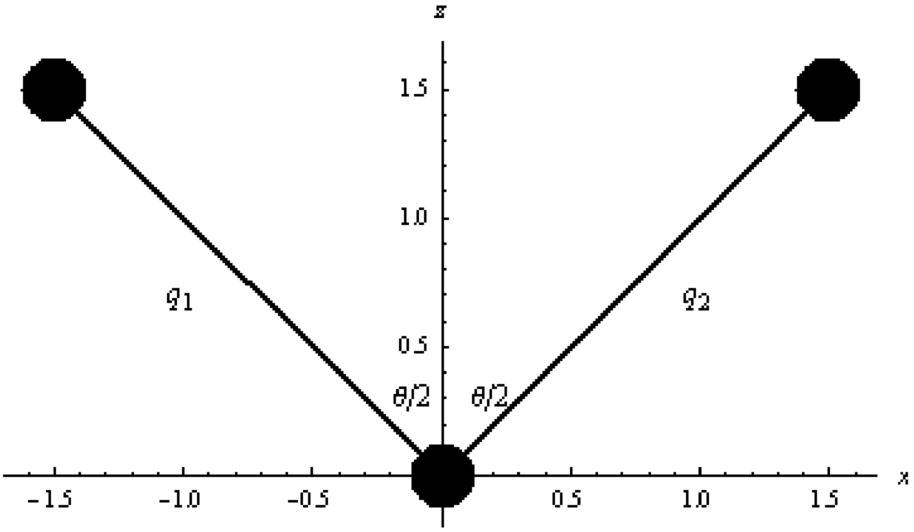

Figure 3.5: Partridge and Schwenke(PS) [33] coordinates system C_3.

1) The PS Function

The choice of the dipole moment functional form is important to describe the correct behaviour.

The PS function is given by

$$\begin{aligned}\vec{\mu}\left(q_2, q_1, \theta\right) &= q\left(q_1, q_2, \theta\right)\left(\vec{x_{\mathrm{C}1}} - \vec{x_{\mathrm{C}2}}\right) + \\ &\quad + q\left(q_2, q_1, \theta\right)\left(\vec{x_{\mathrm{C}3}} - \vec{x_{\mathrm{C}2}}\right) \qquad (3.3.1)\end{aligned}$$

with

$$\begin{aligned}q\left(q_1, q_2, \theta\right) &= \exp(-\beta(q_1 - r_e)^2)\left(\sum_{i=1}^{\mathrm{nr}} \mathrm{C}_i \left(\frac{q_2 - r_e}{r_e}\right)^i\right) \\ &\quad + \exp(-\beta q_1 - r_e)^2) \sum_{ijk} \mathrm{C}_{ijk} \left(\frac{q_2 - r_e}{r_e}\right)^i \left(\frac{q_2 - r_e}{r_e}\right)^j \\ &\quad \times \left(\cos\theta - \cos\theta_e\right)^k \qquad (3.3.2)\end{aligned}$$

with the second sum having:

$$\begin{aligned} i + j + k &\leq n_\theta, & (3.3.3)\\ j + k &> 0, & (3.3.4)\\ i + j &\leq n_r, & (3.3.5)\\ n_r &\leq n_\theta & (3.3.6)\end{aligned}$$

The PS function is controlled by two terms n_r and n_θ and their value is limited by the number of radial and angular points. The parameters C_{ijk} C_i are calculated using a linear least-squares fit. The fit was obtained for q using a Mathematica program written by Lorenzo Lodi (UCL). This is set out in Table 3.3.

During the fitting procedure some points have been added to constrain behaviour in equilateral triangle configurations where a zero dipole moment is expected by symmetry. The final fit chosen has $n_\theta = 7$ and $n_r = 4$, Table 3.3 gives the results. The value used for r_e is 2.46 a.u and θ_e corresponds to the linear configuration.

Table 3.3: AHMPS Fit parameters in a.u, with $n_r = 4$, $n_\theta = 7$ and $\beta = 3.7$

i	j	k	q	i	j	k	q
0	0	0	-0.1854	1	1	0	0.0467
1	0	0	1.0897	1	1	1	15.0394
2	0	0	-6.1417	1	1	2	-102.5349
3	0	0	28.6315	1	1	3	224.6806
4	0	0	-31.7287	1	1	4	-190.0721
0	0	1	0.1920	1	1	5	53.2123
0	0	2	-1.4374	1	2	0	4.5036
0	0	3	7.4693	1	2	1	-177.7461
0	0	4	-17.7946	1	2	2	712.8167
0	0	5	20.8125	1	2	3	-935.1822
0	0	6	-11.8490	1	2	4	387.0837
0	0	7	2.6297	1	3	0	8.2939
0	1	0	-0.2030	1	3	1	-67.2054
0	1	1	-1.4017	1	3	2	-61.9312
0	1	2	10.8417	1	3	3	71.1487
0	1	3	-31.3581	2	0	1	-3.5201
0	1	4	42.5052	2	0	2	64.7173
0	1	5	-28.4328	2	0	3	-172.0531
0	1	6	7.7838	2	0	4	158.1754
0	2	0	0.4010	2	0	5	-46.1796
0	2	1	11.7281	2	1	0	-12.0753
0	2	2	-59.9290	2	1	1	93.3593
0	2	3	123.2878	2	1	2	-367.7184
0	2	4	-104.7863	2	1	3	492.3506
0	2	5	30.5536	2	1	4	-207.8296
0	3	0	-3.9754	2	2	0	-6.0008
0	3	1	-42.3832	2	2	1	-74.5952
0	3	2	108.2957	2	2	2	361.8279

Continued on Next Page…

i	j	k	q	i	j	k	q
0	3	3	-90.6804	2	2	3	-239.6715
0	3	4	24.3682	3	0	1	-28.6117
0	4	0	-23.7117	3	0	2	118.5863
0	4	1	234.0460	3	0	3	-168.7359
0	4	2	-387.7413	3	0	4	67.9076
0	4	3	174.0015	3	1	0	34.6425
1	0	1	0.5393	3	1	1	-336.1718
1	0	2	-7.2829	3	1	2	474.0681
1	0	3	19.9636	3	1	3	-217.1211
1	0	4	-25.0169	4	0	1	-91.5287
1	0	5	16.7842	4	0	2	290.5264
1	0	6	-5.0748	4	0	3	-164.9791

3.3.4 Comparison of DMSs

Having constructed a DMS we are faced with the problem of evaluating how good it is. In order to choose a good DMS we need to perform tests and make comparisons between all data available. The problem is that there are not many experimental or observational absolute intensity measurements. The data available are from Treffers and Gilda [39], Kramer and Jorgesen [37]and Jensen *et al.*. [23].

A program to calculate dipole transition intensities, the DIPOLE3, is available as part of the DVR3DRJ package [1].

Vibrational transition moments reported by Jensen [23] were compared with values obtained using DIPJ0DVR [40]. This program needs as input an accurate and smooth DMS to perform detailed investigations.

Comparison between previous calculations and the new one using the AHM-PART DMS are shown in Table 3.4.

Energy (cm^1)		ν_1	ν_2	l	ν_3	$\nu_1{}'$	$\nu_2{}'$	l'	$\nu_3{}'$	[23]	AHMPART	[39]	[37]
Bra	Ket		Bra				Ket						
0.00	0.00	0	0	0	0	0	0	0	0		0.0491		
2045.72	0.00	0	0	0	1	0	0	0	0	0.3460	0.3198	0.2209	0.3202
2141.49	0.00	0	2	0	1	0	0	0	0	0.0112	0.0961		
2045.72	137.90	0	0	0	1	0	2	0	0	0.0112	0.0623		
2141.49	137.90	0	2	0	1	0	2	0	0	0.3320	0.2773		
2268.92	137.90	0	4	0	1	0	2	0	0	0.0155	0.1145		
2418.37	137.90	0	6	0	1	0	2	0	0	0.0014	0.0240		
3266.00	0.00	1	0	0	1	0	0	0	0		0.0459	0.0552	0.0194

Table 3.4: Transition moments in Debye. Calculations performed using the program DIPJ0 with the DMS built in this work AHMPART compared with previous calculations performed by Jensen et al. [23], Jorgesen calculations [37] and with experimental values obtained by Treffers [39].

The AHMPART DMS shows a good agreement with all data available and this is the one I recommend using to perform the C_3 transition intensity calculations. Calculations using the AHMPART DMS fit with DIPOLE3 module and comparison with previous calculations performed by Jensen [23] are shown in Table 3.5

In conclusion, a wide overview of the C_3 molecular system and all preparatory work for line list calculation have been described. Future work will involve performing other necessary tests and starting the actual calculations to complete this line list computational project.

Energy (cm^{-1})		ν_1	ν_2	l	ν_3	$\nu_1{}'$	$\nu_2{}'$	l'	$\nu_3{}'$	[23]	AHMPART
Bra	Ket		Bra				Ket				
0.85	0.00	0	0	1	0	0	0	0	0		0.0384
68.00	0.00	0	1	1	0	0	0	0	0	0.4371	0.4115
214.70	0.00	0	3	1	0	0	0	0	0	0.0131	0.0291
137.90	68.00	0	2	0	0	0	1	1	0	0.3513	0.3529
295.30	68.00	0	4	0	0	0	1	1	0	0.0185	0.0288
469.03	68.00	0	6	0	0	0	1	1	0	0.0020	0.0041
214.70	137.90	0	3	1	0	0	2	0	0	0.4902	0.4735
380.13	137.90	0	5	1	0	0	2	0	0	0.0288	0.0424
561.40	137.90	0	7	1	0	0	2	0	0	0.0041	0.0067
1320.47	0.00	1	1	1	0	0	0	0	0	0.0167	0.0050
1504.41	0.00	1	3	1	0	0	0	0	0	0.0022	0.0027
1226.70	68.00	1	0	0	0	0	1	1	0	0.0167	0.0005
1410.00	68.00	1	2	0	0	0	1	1	0	0.0165	0.0075
1597.65	68.00	1	4	0	0	0	1	1	0	0.0016	0.0034
1320.00	137.90	1	1	1	0	0	2	0	0	0.0165	0.0017
1504.41	137.90	1	3	1	0	0	2	0	0	0.0230	0.0110
1696.23	137.90	1	5	1	0	0	2	0	0	0.0210	0.0049

Table 3.5: Calculations obtained with DIPOLE3 program using as input the AHPART DMS are compared with calculations performed by Jensen [23]

Chapter 4

Conclusion

4.1 Summary

In conclusion, a wide overview of the C_3 molecular system and all preparatory work for line list calculation have been described. The preparatory work for calculating the C_3 line list aimed to carry out testing procedures and building analytical tools needed to develop the final calculations for the line list. Investigations of properties of this molecule and theoretical calculations of its infrared absorption spectrum are important for determining some essential parameters used in modelling reliable dynamics of atmospheres of cool C-rich stars. The program used to calculate C_3 energy levels (DVR3D) needs as input a Potential Energy Surface (PES). This function describes the electron energy distribution for each nuclear configuration. The quality of the PES determines the accuracy of the energy level calculations. In order to select the most reliable, tests on two C_3 PESs taken from the literature have been performed. Energy level convergency tests have been carried out and DVR3D parameter optimization has been described. Further, a dipole moment surface (DMS) was built fitting ab-initio dipole component points [19] using a PS functional form [33]. The DMS can be used in DVR3D to determine the transition intensities. What is next?

4.2 Future Work

Future work will involve performing other necessary tests and starting the actual calculations to complete this line list computational project. First, it will be necessary to test and choose the value for IBASS as explained in the last section. This is the only parameter left to test in DVR3D before starting performing energy level calculations. The output file printed out running ROTLEV is used by the DIPOLE module to perform transition intensity calculations. The parameters to set in DIPOLE are the number of eigenfunctions considered and the energy of the ground state [1]. Calculations of a large enough number of energy levels allows the use of Boltzmann statistics to determine partition functions. It is the module SPECTRA in DVR3D that allows one to perform those calculations. Accurate opacity value for C_3 could allow a better modeling of atmospheric dynamics in those stars where C_3 molecules play an important role. I hope the preparatory work explained in this report can support future work.

References

[1] J. Tennyson et al. DVR3D: a program suite for the calculation of rotation-vibration spectra of triatomic molecules. *Comput. Phys. Commun.*, 163:85–116, 2004.

[2] G. Duxbury. *Infrared Vibation-Rotation Spectroscopy.* John Wiley and Sons, 2000.

[3] Wikipedia. Technical report. http://en.wikipedia.org/wiki/.

[4] R. Bigoni. Technical report. http://www.robertobigoni.it/Fisica.

[5] L. Patern. Astrofisica. Academic Notes, 2001.

[6] D. Bhattacharya. Technical report. http://www.rri.res.in/ dipankar/ph217/transport.pdf.

[7] Carbon molecules, ions, and clusters. *The Astrophysics Spectator*, 2.21, 2005.

[8] U. G Jorgesen. *Rev. Mexicana Astron. Astrf.*, 23:49–62, 1992.

[9] A. Braccesi. *Dalle stelle all'universo, lezioni di Astrofisica.* Zanichelli, 2000.

[10] W. Weltner and R. J. Van Zee. Carbon molecules, ions, and clusters. *Chem. Rev.*, 89:1713–1747, 1989.

[11] T. F. Giensen, A. O. Van Orden, J. D. Cruzan, R. A. Provencal, R. J. Saykally, R. Gendriech, F. Lewen, and G. Winnewisser. *Ap. J. Lett.*, 555, 2001.

[12] J.R. Goicoechea and J. Cernicharo. Spectroscopy of key molecular species in the infrared. *ApJ*, 2001.

[13] J. M. Hollas. *Modern Spectroscopy.*

[14] P. R. Bunker. Quasiliner and quasiplanar molecule. *Ann. Rev. Phys. Chem.*, 1983.

[15] W. P. Kraemer. A theoretical study of the rotation-vibration energy levels and dipole moment functions of CCN^+, CNC^+ and C_3. *J. Mol. Spectrosc.*, 107:191–207, 1984.

[16] F. J. Northrup and T. J. Sears. Stimulated-emission pumping spectrocscopy study of jet-cooled C_3: pure bending levels and bend-symmetric combination levels of $\widetilde{X}\Sigma_g^+$. *J. Opt. Soc. Am.*, 7:1924–1933, 1990.

[17] E. A Rohlfing and J. E. M. Goldsmith. Stimulated-emission pumping spectroscopy of jet-cooled C_3: antisymmetric stretch-bent levels. *J. Opt. Soc. Am.*, 7:1915–1923, 1990.

[18] F. J. Northrup, T. J. Sears, and E. A. Rohlfing. A semirigid bender analysis of an extensive set of rotation-vibration levels in $\widetilde{X}\Sigma_g^+$ of C_3. *J. Mol. Spectrosc.*, 145:74–88, 1991.

[19] K. G. Ahmed, G. Balint-Kurti, and C. M. Western. Ab initio calculations and vibrational energy level fits for the lower singlet potential-energy surfaces of C_3. *J. Chem. Phys*, 121:10041, 2004.

[20] F. J. Northrup and T. J. Sears. Observation ofstimulated emission pumping spectra of jet-cooled C_3. *Chem. Phys. Lett.*, 159:421–425, 1989.

[21] E. A. Rohlfing and J. E. M. Goldsmith. Stimulated-emission pumping spectroscopy of jet-cooled C_3. *J. Chem. Phys.*, 90:6804, 1989.

[22] C. A. Schmuttenmaer, R. C. Cohen, N. Pugliano, J. R. Heath, A. L. Cooksy, K. L. Busarow, and R. J. Saykally. Tunable far-ir laser spectroscopy of jet-cooled carbon clusters: The ν_2 bending vibration of C_3. *Science*, 249:897–900, 1990.

[23] P. Jensen, C. Rohlfing, and J. Almof. Calculation of the complete-active-space self-consistent-field potential-energy-surface, the dipole moment surfaces, the rotation-vibration energies, and the vibrational transition moments for C_3. *J. Chem. Phys.*, 97:3399, 1992.

[24] G. Zhang, K. S. Chen, A. J. Merer, Y. C. Hsu, W. J. Chen, S. Shaji, and Y. A. Liao. The 4051-*a* band of C_3:perturbated low-j lines and life time measurament. *J. Chem. Phys.*, 122:1–8, 2005.

[25] A. D. Walsh. *Discuss. Farday Soc.*, 35, 1963.

[26] J. J. Keady et al. The IRC+10216 circumstellar envelope models forthe dust and gas. *ApJ*, 326:832–842, 1988.

[27] K. W. Hinkle, J. J. Keady, and P. B. Bernath. Detenction of C_3 in the circumstellar shell of irc+10216. *Science*, 242:1319–1322, 1988.

[28] J. Cernicharo and J. R. Goicoechea. Far-infrared detection of C_3 in sagittarius B2 and IRC+10216. *ApJ*, 534:199–202, 2000.

[29] G. J. Harris, J. Tennyson, B. M. Kaminski, Ya. V. Pavlenco, and H. R. A. Jones. Improved HCN/HNC linelist, model atmospheres and synthetic spectra for WZ Cas. $Mon.Not.R.Astron.Soc.$, $InPress$, 2006.

[30] P. Jensen and P. R. Bunker. *Computational molecular Spectroscopy.* John Wiley and Sons, 2000.

[31] O. L. Polyansky, A. G Csszr, Shirin S. V., Zobov N. F., P. Barletta, J. Tennyson, D. W. Schwenke, and Knowles P. J. High-accuracy ab initio rotation-vibratio transitions for water. *Science*, 299:539–542, 2003.

[32] J. Werner and P.J. Knowles. MORPLO, a package of ab-initio programs. 2002.

[33] H. Partridge and D. W. Schwenke. The determination of accurate isotope potential anergy surface for water from extensive ab initio calculations and experimental data. *J. Chem. Phys.*, 106:4618, 1997.

[34] M. Mladenovic, S. Schmatz, and P. Botschwina. Large-scale ab initio calculations for C_3. *J. Chem. Phys*, 101:5891, 1994.

[35] K. Kawaguchi, K. Matsumura, H. Kanamori, and E. Hirota. Diode laser spectroscopy of C_3: The $\nu_2 + \nu_3 - \nu_2$, $2\nu_2 + \nu_3 - 2\nu_2$ and $2\nu_2 + \nu_3$ bands. *J. Chem. Phys.*, 91:1953–1957, 1989.

[36] J. Baker. Observation of new bands in the lasr induced fluorescence spectrum of C_3. *J. Mol. Spectrosc.*, 183:6–11, 1997.

[37] U. G. Jorgesen, J. Almlof, P. Siegbahn, and M. F. Affiliation. *ApJ*, 343:554–561, 1989.

[38] J. Almof, C. W. Bauschlicher, P. E. M. Siegbahn, B. O. Roos, A. Heinberg, P. R. Taylor, Malmqvist P. A., and Rendell A. P. MOLECULAR SWEDEN.

[39] R. R. Trefferes and D. P. Girla. *Ap.J.*, 202, 1975.

[40] J. R. Henderson, C. R. Le Suer, and J. Tennyson. DVR3D:programs for fully pointwise calculation of vibrational spectra. 2006.

[41] D. H. Liskow, C. F. Bender, and H. F. Schaefer. *J. Chem. Phys.*, 56:5075–5080, 1972.

[42] B.J. McCall, R.N. Casaes, M. Adamkovics, and R.J. Saykally. A reexamination of the 4051 $\AA$ band of C_3 using cavity ringdown spectroscopy of a supersonic plasma. *Chem. Phys. Lett.*, 374:583–586, 2003.

[43] A. Tanabashi, T. Hirao, and T. Amano. Fourier trasform emission spectra of the (000)-(000) band of the 4051.6 $\AA$ band of C_3. *ApJ*, 624:1116–1120, 2005.

[44] J. Szczepanski, S. Ekern, and M. Vala. Vibrational spectroscopy of small matrix-isolated linear carbon cluster anions. *J. Phys. Chem.*, 101:1841–1847, 1997.

[45] J. Szczepanski, H. Wang, and M. Vala. Reaction of the C_3 carbon cluster with benzene. *Chem. Phys.*, 303:165–177, 2003.

[46] E. A. Rohlfing. Laser-induced-fluorescence spectrroscopy of jet-cooled C_3. *J. Chem. Phys.*, 91:6804, 1989.

[47] D. W. Schwenke and H. Partridge. Convergence testing of analytic representation of ab initio dipole moment function for water: Improved fitting yields improved intensities. *J. Chem. Phys.*, 113:6592–6597, 2000.

[48] V. Spirko and P. Jensen. Calculation of rotation-vibration energy levels in ground state C_3 by born-oppenheimer-type separation of the vibrational motions. *J. Mol. Spectrosc.*, 183:128–138, 1997.

[49] I. Plesser and Z. Vager. Structure of C_3 as measured by the Coulomb-Explosion technique. *Phys. Rev. Lett.*, 56:1559, 1986.

[50] R. Loidl, J. Hron, U. G. Jorgens, and S. Hofner. Proibing the outer atmosphere of carbon stars. C_2, H_2, HCN and C_3 features in the SWS range. *AA*, 56:1559, 1986.

[51] L. Gausset, G. Herzberg, A. Lagerqvist, and B. Rosen. *ApJ*, 142, 1965.

[52] B. T. Sutcliffe and J. Tennyson. *Internat. J. Quantum Chem.*, 39:183–196, 1991.

[53] O. Takeshi, J. A. Thorburn, B. J. McCall, S. D. Friedman, L. M Hobbs, P. Sonnentrucker, D. E Welty, and D. G York. Observations of C_3 in translucent slight light. *ApJ*, 582:823–829, 2003.

[54] R. Gendriech, T. F. Giensen, F. Lewen, and G. Winnewisser. Terahertz spectroscopy of linear triatomic ccc: High precision laboratory measurament and analysis of the ro-vibrational bending transitions. *Z.Naturforsch.*, 58a:129–138, 2003.

[55] A. E. Lynas-Gray, S. Miller, and J. Tennyson. Infrared transition intensities for water: A comparison of ab initio and fitted dipole moment surfaces. *J. Mol. Spectrosc.*, pages 458–467, 1995.

[56] R. G. LittleJohn, K. Mitchell, V. Aquilanti, and S. Cavalli. Body frames and frame singularities for three-atom systems. *Phys. Rev. A*, 58:3705–3717, 1998.

[57] P. Jensen. Calculation of rotation-vibration linestrengths for triatomic molecules using a variational approach. *J. Mol. Spectrosc.*, 132:429–457, 1988.

[58] K. J. Higgins, S. M. Freund, W. Klemperer, A. J. Apponi, and L. M. Ziurys. The rotational spectrum and dynamical structure of LIOH and LiOD: A combined laboratory and ab initio study. *J. Chem. Phys.*, 121:11715, 2004.

[59] R. J. Barber, J. Tennyson, G. J. Harris, and R. N. Tolchenov. A high accuracy computed water line list. *Mon. Not. R. Astron. Soc.*, 368, 2005.

[60] P. De Laverny, C. Abia, B. Domnguez I., Plez, O. Straniero, R. Wahlin, K. Eriksson, and Jrgensen U. G. Chemical analysis of carbon stars in the local group. *Astronomy and Astrophysics manuscript*, 446:1107–1118, 2006.

[61] J. A. Fernley, S. Miller, and J. Tennyson. *J. Mol. Spectrosc.*, 150:597–609, 1991.

[62] C. R. Le Sueur, S. Miller, and J. Tennyson. On the use of variational wavefunctions in calculating vibrational band intensities. *Mol. Phys.*, 76:1147–1156, 1992.

[63] J. R. Henderson and J. Tennyson. All the vibrational bound states of H_3^+. *Chem. Phys. Lett.*, 173:133–138, 1990.

[64] H. Y. Mussa and J. Tennyson. Calculation of the rotation-vibration states of water up to dissociation. *J. Chem. Phys.*, 109:10885, 1998.

[65] J. Makarewicz. Rovibrational hamiltonian of a triatomic molecule in local and collective internal coordinates. *J. Phys. B:At. Mol. Opt. Phys.*, 21:1803–1819, 1988.

[66] F Wang. *Ab initio calculations of rotovibrational states of alkali metal ions.* PhD thesis, Departmant of Chemistry, The University of Newcastle, 1994.

[67] D. W. Schwenke and H. Partridge. *J. Chem. Phys.*, 113, 2000.

[68] T. Giensen. Molecular astrophysics: The search for interstellar carbon clusters. Technical report, Physikalisches Institut Universitat Zu Koln, 2002.

[69] G. Larsson. The C_3 molecule: A litterature study and spectroscopic investigation in flames and on graphite. Technical report, Lund Institute of Technology, 2002.

[70] G. J Harris. *An ab initio HCN/HNC Rotational-Vibrational Line List and Opacity Function for Astronomy.* PhD thesis, Department of Physics and Astronomy University of London, 2002.

[71] M. L Abell. *Statistics with mathematica.* Academic Press, 1999.

[72] P. W. Atkins and R. S. Friedman. *Molecular Quantum Mechanics. Third Ediction.* Zanichelli, 1997.

[73] C. N. Banwell. *Fundamentals of Molecular Spectroscopy.* McGraw-hill Book Company, 1972.

[74] J. D. Graybeal. *Molecular Spectroscopy.* International editions, 1988.